RITARS-11-H-UVA

Sinkhole Detection, Landslide and Bridge Monitoring for Transportation Infrastructure by Automated Analysis of Interferometric Synthetic Aperture Radar Imagery

Final Report

Principal Investigator:

Prof. Scott Acton

University of Virginia

Program Manager:

Mr. Caesar Singh

Research Innovative Technology Administration

U.S. Department of Transportation

Executive summary

During the two year project, a series of radar satellite data were collected and processed by TRE Canada scenes using interferometric synthetic aperture radar (InSAR) technology into ground displacement measurements. These displacement data, with accuracy below 1 cm and approaching 1 mm, provided the initial data with which to study phenomena affecting transportation in Virginia. The phenomena analyzed included subsidence due to sinkhole formation, movements due to landslides and rockslides, and bridge settlement. The study area was comprised by a 40km by 40km region near Middlebrook, Virginia. Additional data outside of Virginia (from Vancouver, Canada and Wink, Texas) provided by TRE Canada proved useful in prototyping and validating the image analysis algorithms.

A focus of the project was the development of image analysis algorithms that take the InSAR data as input and provide outputs of detections that can be used in a decision support system (DSS) to identify potential hazards to transportation. Two main theoretical approaches were explored: a graph-theoretic approach and parametric approach. In the graph theory approach, regions of subsidence were identified by an optimization process. This approach however was limited and did not allow for an easy integration of the main feature offered by the InSAR acquisition: the displacement time history for each scatterer. The second more generalized parametric approach exploited the temporal dimension as well as the spatial data. This approach is based on the availability of models describing both the spatial and temporal behavior of the geophysical features of interest. The model parameters are used to generate a multidimensional space that is then scanned with user-defined resolution. For each point in the parameter space, a spatiotemporal template is reconstructed from the original model. This template is then used to scan the point cloud data set for regions matching the spatiotemporal behavior. This new parametric approach provides the flexibility necessary to allow extensibility to other geophysical phenomena of interest.

Photogrammetry, LiDAR, as well as traditional surveying methods were used as comparison to the InSAR-driven results and these ground studies confirmed and validated the results achieved from remote sensing. This final report details a number of case studies and inspections performed by the Virginia Department of Transportation (VDOT) including cases of sinkhole formation, bridge settlement and rockslides. In terms of automated geohazard detection (as provided by the newly developed algorithms operating on the InSAR data acquired over Virginia), the ground studies show that about 78% of the cases identified by our algorithm present strong field evidence of subsidence.

Acknowledgements

We wish to acknowledge the participants in this project.

For the University of Virginia (UVA) team, Dr. Scott Acton served as principal investigator and led the research in image analysis. Andrea Vaccari was the lead researcher and, along with Michael Stuecheli, developed algorithms that enabled analysis of geohazards and bridge displacement. Mr. Vaccari also performed the majority of reporting and documentation duties. Dr. Qian Sang was the UVA contributor to the cost-benefit analysis.

Dr. Edward Hoppe led the Virginia Center for Transportation Innovation and Research (VCITR). This Virginia Department of Transportation (VDOT) center perform ground studies and validation. In this work, Dr. Bruckno was the lead geologist. Stacey Provence-Roosa performed LiDAR studies, and Dr. William Niemann (Marshall U.) performed photogrammetric studies. Other personnel resources included Elizabeth Campbell (geographical information systems) and Audrey Moruza (cost-benefit analysis).

The TRE-Canada team was led by CEO Adrian Bohane. Dr. Giacomo Falorni provided data analysis and technical assistance on remote sensing. Geographical information system expertise was added by Jessica Morgan.

The technical advisory board consisted of: Dr. Scott Anderson (FHWA), Dr. Khan M. Iftekharuddin (VCU), Mr. Rodolfo Maruri (FHWA), Dr. Keith Cunningham (U. Alaska), Dr. Colin Brooks (Michigan Tech) and Dr. Al Bovik (UT-Austin).

Disclaimer

The views, opinions, findings and conclusions reflected in this paper are the responsibility of the authors only and do not represent the official policy or position of the USDOT/RITA, or any State or other entity.

Glossary

AOI	**A**rea **O**f **I**nterest
CSK	**C**OSMO-**SK**yMed
DEM	**D**igital **E**levation **M**odel
DInSAR	**D**ifferential **InSAR**
DOT	**D**epartment **O**f **T**ransportation
DS	**D**istributed **S**catterer
FHWA	**F**ederal **H**igh**W**ay **A**dministration
GIS	**G**eographic **I**nformation **S**ystem
IEEE	**I**nstitute of **E**lectrical and **E**lectronics **E**ngineers
InSAR	**In**terferometric **S**ynthetic **A**perture **R**adar
LiDAR	**Li**ght **D**etection **A**nd **R**anging
LOS	**L**ine-**O**f-**S**ight
NED	**N**ational **E**levation **D**ataset
PS	**P**ermanent **S**catterer
PSInSAR	**P**ermanent **S**catterer **InSAR**
RADAR	**RA**dio **D**etection **A**nd **R**anging
SAR	**S**ynthetic **A**perture **R**ADAR
SSIAI	IEEE **S**outhwest **S**ymposium on **I**mage **A**nalysis and **I**nterpretation
TRE	**TRE** Canada
TS	**T**emporary **S**catterer
USGS	**U.S. G**eological **S**urvey
UVA	**U**niversity **O**f **V**irginia
VDOT	**V**irginia **D**epartment **O**f **T**ransportation
VIVA	**V**irginia **I**mage and **V**ideo **A**nalysis
VCTIR	**V**irginia **C**enter for **T**ransportation **I**nnovation & **R**esearch
VRTC	**V**irginia **R**esearch **T**ransportation **C**ouncil

Table of contents

List of figures

List of tables

Introduction

Background

The Virginia Image and Video Analysis (VIVA) laboratory at the University of Virginia (UVA) is leading a research project with the Virginia Department of Transportation (VDOT) and TRE Canada entitled "Sinkhole Detection, Landslide and Bridge Monitoring for Transportation Infrastructure by Automated Analysis of Interferometric Synthetic Aperture Radar Imagery" (BAA No. RITARS-11-H-UVA). The work was awarded to the University of Virginia as a research grant funded by the Commercial Remote Sensing and Spatial Information Technology Application Program.

One of the main objectives of this project is to determine whether InSAR data can be used to detect and monitor geohazards and movement occurring over infrastructure. The use of advanced remote sensing technologies to identify unstable areas would have the potential to assist the transportation community with increasing public safety and reducing the occurrence of emergency repairs which have higher associated costs than standard maintenance. Under this main objective, other objectives included developing software to identify geohazards relevant to transportation and ground validation of these algorithms.

TRE Canada Inc. (TRE) has been contracted to perform the InSAR component of this project over an area totaling 1,600 kilometers squared in size, centered over the town of Middlebrook, Virginia. InSAR monitoring was carried out using TRE's proprietary SqueeSAR™ algorithm. COSMO-SkyMed (CSK) imagery was used for this monitoring project due to the high spatial resolution and acquisition frequency of the CSK satellites.

The Virginia Center for Transportation Innovation and Research (VCTIR) was selected as second subcontractor for this project. VCTIR is a collaboration between the Virginia Department of Transportation and the University of Virginia dating back to 1948. VCTIR had the responsibility for identifying study areas, performing on-site analysis and baseline verification, cost-benefit analysis as well as evaluating GIS tools for integration of the analysis results obtained by the project into VDOT framework. Along with the parent organization VDOT, VCTIR provided the necessary facilities in GIS management, photogrammetry, LiDAR and expertise in geology.

Tasks

Reporting

In terms of reporting, the technical milestones and financial status were reported each quarter. Furthermore, oral presentations were given in Washington, D.C. at the U.S. DOT as proposed. Technical presentations at TRB and other meetings were also performed by the project team.

For more information about the outreach activities see Publications and Outreach.

Acquisition and pre-processing of remotely sensed imagery

Area of interest

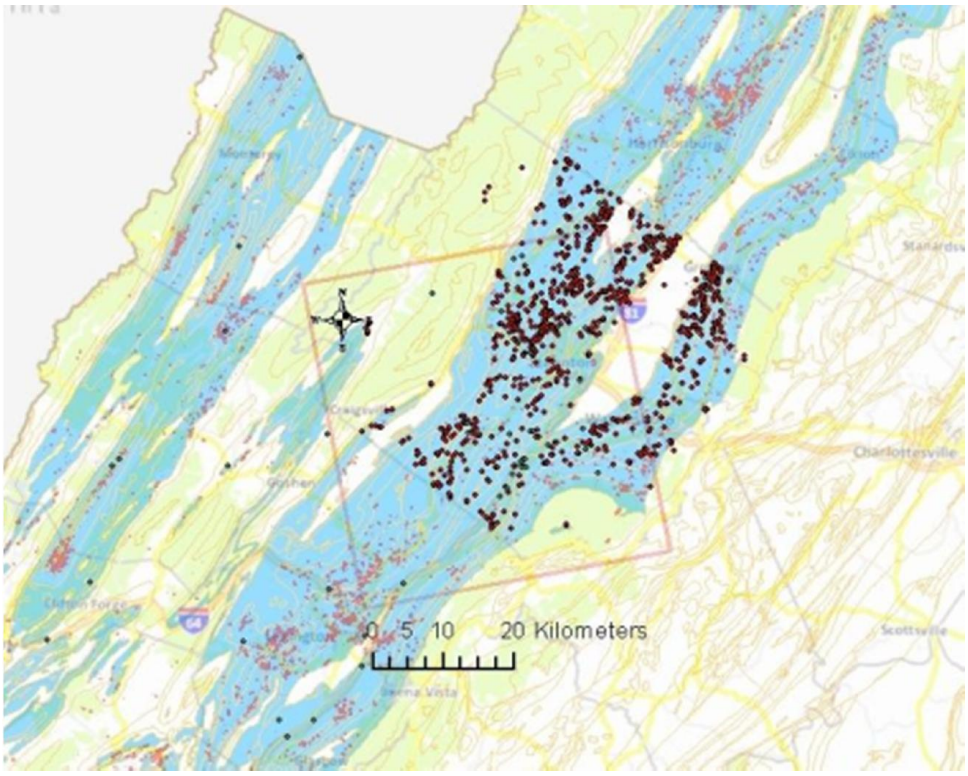

Figure 1 - Area of interest.

The area of interest (AOI) selected for our study is a region of about 40x40 km (618 miles^2) chosen because of the diversity of geological conditions. The area, represented in Figure 1, is centered roughly on the locality of Middlebrook, Augusta County, Virginia, and is a tectonically complex area spanning the Valley and Ridge and Blue Ridge physiographic provinces [1].

Geological ages ranging from Holocene sediments to Precambrian granulite gneiss [2], with frequent nonconformities, are represented within the AOI. The predominant tectonic framework consists of eastward-dipping thrust faults and decollements related to repeated orogenic cycles [3]. The AOI contains carbonate, non-carbonate clastic, and metamorphic terrains, resulting in both rock slope stability and karst geohazards. The karst areas range in age from Cambrian to Devonian and formed during the Taconic and Acadian Orogenies and their associated divergent and inter-orogenic periods. Karst lithologies consist mainly of limestone and dolostone, while non-carbonate clastic lithologies consist of occasionally interbedded shales, siltstone, conglomerates and sandstone, and the metamorphic lithologies consist of charnockite, granulite gneiss, quartzite, and greenschist and blueschist-grade metabasalt. Figure 1 illustrates karst terrains in light blue, with areas of known sinkhole locations and previously-repaired sinkholes located in red.

From a radar imaging point of view, the environment of the AOI is mixed between dense vegetation, active agriculture, fallow fields, exposed ground, infrastructure and

towns. Mountainous terrain and areas of highly variable topography are present in the northwest and southeast corners of the scene. Man-made structures, bare or sparsely vegetated ground often yield a high number of measurement points. In contrast, areas of dense vegetation, active agriculture and steep slopes often produce a low density of measurement points.

Technology

The project was based on the use of a technology known as interferometric synthetic aperture radar (InSAR). This technology allows the derivation of very accurate ground deformation measurement from space borne platforms.

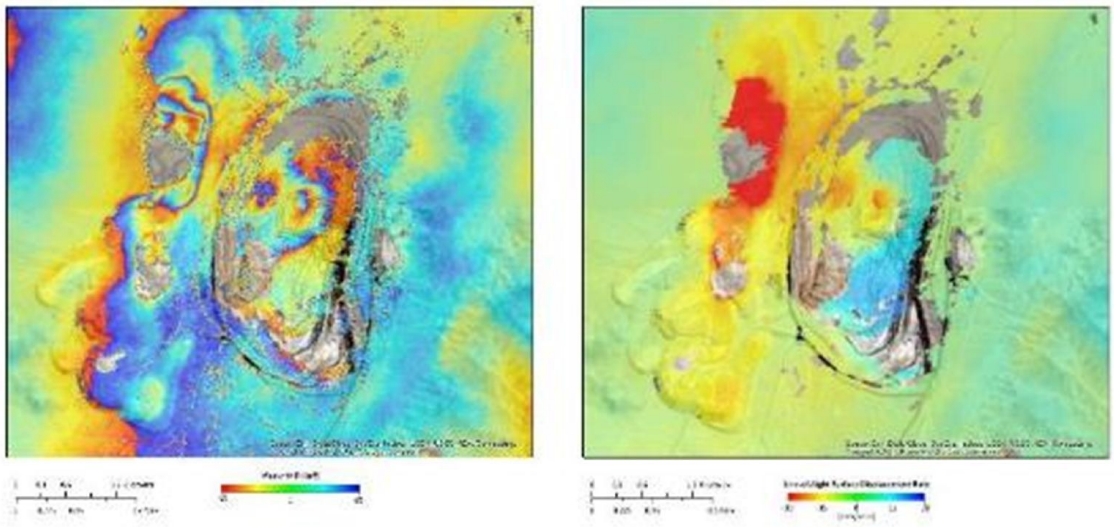

Figure 2 - Example of InSAR interferogram (left) and deformation map derived from it (right).

InSAR

InSAR, also referred to as SAR interferometry, is the measurement of signal phase change (interference) between radar images. When a point on the ground moves, the distance between the sensor and the point changes, thereby producing a corresponding shift in signal phase. This shift is used to quantify the ground movement. An interferogram is a 2D representation of the difference in phase values. Variations of phase in an interferogram are identified by fringes, colored bands that indicate location and extent of movement. The precision with which the movement can be measured is usually in the centimeter range as the phase shift is also impacted by topographic distortions, atmospheric effects, and other sources of noise.

Differential InSAR (DInSAR) and deformation maps

When InSAR is used to identify and quantify ground movement, the process is referred to as Differential InSAR (DInSAR). In DInSAR topographic effects are removed by using a Digital Elevation Model (DEM) of the area of interest to create a differential interferogram that is then converted into a deformation map by transforming the phase values to ground deformation in the satellite Line-Of-Sight (LOS). Only interferograms with good coherence can be converted into a deformation map. Although DInSAR is still

impacted by atmospheric effects, as there is no method for removing this signal phase contribution, it is nevertheless a useful tool for identifying footprints of progressing movement and creating deformation maps. The limitation of DInSAR is its relatively low precision (centimeter scale) and that it cannot distinguish between linear and non-linear motion.

Permanent Scatterer InSAR (PSInSAR™)

PSInSAR™ [4] is an advanced form of DInSAR. The fundamental difference is that it uses multiple interferograms created from a stack of at least 15 radar images. PSInSAR™ was developed to overcome the errors produced by atmospheric artifacts on signal phase. The PSInSAR™ algorithm automatically searches the interferograms for pixels that display stable radar reflectivity characteristics throughout every image of the dataset. In PSInSAR™ these pixels are referred to as Permanent Scatterer(s) (PS). The result is the identification of a sparse grid of point-like targets on which an atmospheric correction procedure can be performed. Once these errors are removed, a history of motion can be created for each target, allowing the detection of both linear and non-linear motion.

The result is a sparse grid of PS that are color-coded according to their deformation rate and direction of movement. The information available for each PS includes its deformation rate, acceleration, total deformation, elevation, coherence as well as a time series of movement. PSInSAR™ measures ground movement with millimeter accuracy.

SqueeSAR™

PSs are objects, such as buildings, fences, lampposts, transmission towers, crash barriers, rocky outcrops, etc, that are excellent reflectors of radar microwaves. However, TRE has noticed that many other signals are present in the processed data. These do not produce the same high signal-to-noise ratios of PS but are nonetheless distinguishable from the background noise. Upon further investigation it was found that the signals are reflected from extensive homogeneous areas where the back-scattered energy is less strong, but statistically consistent. These areas have been called distributed scatterer(s) (DS) and correspond to rangeland, pastures, bare earth, scree, debris fields, arid environments, etc.

The SqueeSAR™ algorithm [5] was developed to process the signals reflected from these areas. As SqueeSAR™ incorporates PSInSAR™ no information is lost and movement measurement accuracy is unchanged. SqueeSAR™ also produces improvements in the quality of the displacement time series. The homogeneous areas that produce DS normally comprise several pixels. The single time series attributed to each DS is estimated by averaging the time series of all pixels within the DS, effectively reducing noise in the data.

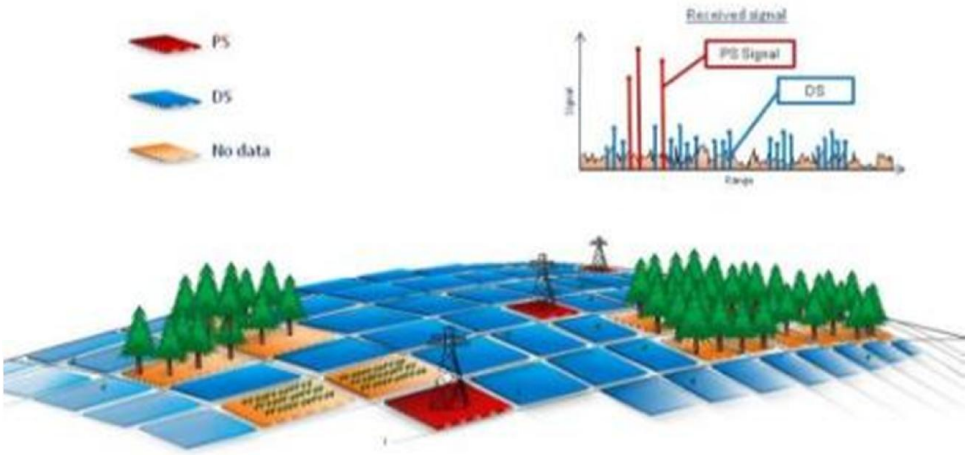

Figure 3 - Illustration of the identification of PS and DS as obtained by application of SqueeSAR.

Temporary Scatterer

To address some of the requirements of this project, an innovative technique known as Temporary Coherence Scatterer(s) (TS) was developed by TRE. This technique examines information on a point-by-point basis (every cell of data within the radar scene). In this advanced approach, each image pair (interferogram) within the entire data tack is examined and any coherent information is extracted. The result is a single image representing information measured from all coherent data contained throughout the entire stack. The technique works by removing the constraint that every point must remain coherent throughout the entire stack of radar scenes (critical in the SqueeSAR algorithm). This relaxation of the coherence paradigm typically leads to a greater spatial coverage of the results, including over areas where PS and DS cannot be identified.

The output is a non-continuous raster map representing average surface displacement rates. The TS approach represents a more robust solution for increasing the density of ground deformation data compared to a simple relaxation of coherence thresholds. As TS are actually pixels in which several points are averaged, noise is suppressed, while a simple reduction of the coherence threshold for the selection of PS/DS would introduce lower quality points into the analysis. Reliable ground motion would be difficult to extract from these low coherence points as time series would be noisier and difficult to interpret. The use of the TS approach assisted in the detection and delineation of unstable areas.

It is important to note that there are several limitations inherent to this approach. First, it is not known which scenes contribute information to any particular TS. As a result, the time interval over which ground displacement occurs is unknown and may vary across the end result. Furthermore, as numerous interferograms are used, the time of year may also fluctuate among these data cells. Finally, as the product of a TS analysis is static, no time series information can be extracted.

Figure 4 - Comparison between the PS and DS results (left) and the TS results (right). Note the subsidence areas identified on the right by the use of the TS technique.

Data acquisition

Geometry

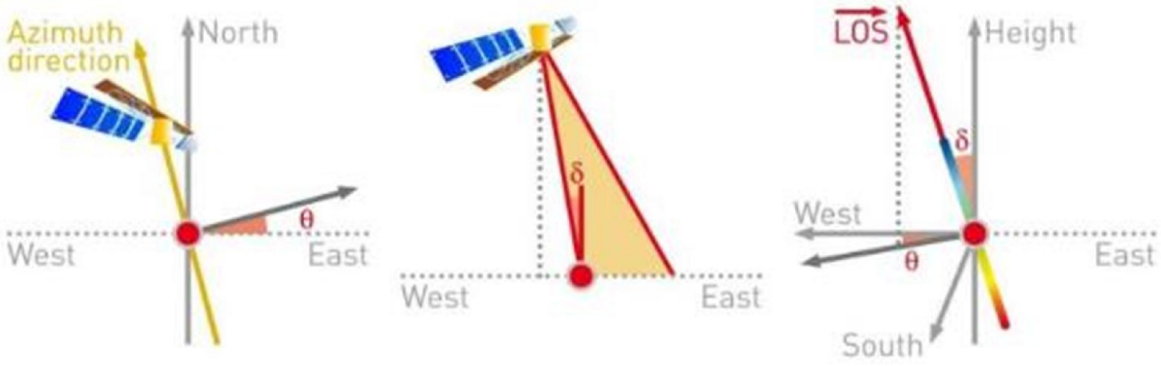

Figure 5 - Geometry of the satellite image acquisition over the AOI.

InSAR-based approaches measure surface displacement on a one-dimensional plane, along the satellite line-of-sight (LOS). The LOS angle varies depending on the satellite and on the acquisition parameters while another important angle, between the orbit direction and the geographic North, is nearly constant.

All CSK images for this project analysis were acquired from an ascending orbit (satellite travelling from south to north and imaging to the east) in beam mode H4-0B. The symbol $\delta = 24.24°$ represents the angle the LOS forms with the vertical and $\theta = 12.51°$ the angle formed with the geographic north (Figure 5).

Schedule

The data processed for this stage of the monitoring project included all images scheduled for acquisition over this area. A total of 32 images acquired between 29 August 2011 and 25 October 2012 were processed, representing fourteen months of monitoring over the area of interest.

Table 1 - Dates of acquired images over AOI.

No.	Date	No.	Date	No.	Date	No.	Date
1	29 Aug 2011	**9**	17 Nov 2011	**17**	23 Mar 2012	**25**	19 Jun 2012
2	05 Sept 2011	**10**	02 Dec 2011	**18**	08 Apr 2012	**26**	05 Jul 2012
3	13 Sept 2011	**11**	18 Dec 2011	**19**	16 Apr 2012	**27**	21 Jul 2012
4	21 Sept 2011	**12**	03 Jan 2012	**20**	02 May 2012	**28**	06 Aug 2012
5	29 Sept 2011	**13**	19 Jan 2012	**21**	18 May 2012	**29**	22 Aug 2012
6	07 Oct 2011	**14**	04 Feb 2012	**22**	11 Jun 2012	**30**	23 Sep 2012
7	15 Oct 2011	**15**	20 Feb 2012	**23**	12 Jun 2012	**31**	09 Oct 2012
8	31 Oct 2011	**16**	07 Mar 2012	**24**	15 Jun 2012	**32**	25 Oct 2012

Accuracy and density

Table 2 - Comparison between the two acquisition campaigns over the two clusters within the AOI.

Attribute	2011		2012	
	Cluster 1	Cluster 2	Cluster 1	Cluster 2
Number of images processed	16	16	32	32
Time period covered (months)	6	6	14	14
Number of PS	38,057	336	166,348	1,453
Number of DS	148,536	2,486	129,773	1,512
Total number of scatterer (PS+DS)	186,593	2,822	296,121	2,695
Density (scatterer/mile^2)	307	307	484	484
Average displacement rate (mm/year)	2.05	0.57	0.23	-0.21
Average displacement rate standard deviation (mm/year)	3.38	8.67	1.50	1.36
Average acceleration rate (mm/year^2)	8.61	62.94	0.45	-3.49
Average acceleration rate standard deviation (mm/year^2)	50.32	129.37	9.61	8.70

A density of 484 PSs and DSs per square mile was achieved from the SqueeSAR analysis of the CSK radar imagery, representing a 58% increase from the result reported during the project (Table 2). The increase in the number of points, particularly the point scatterers, was due to the improvement in the statistical robustness of the data processing caused by the processing of a larger data stack acquired over a longer period of time. The precision of the 2012 results also improved considerably (Table 2).

Data processing

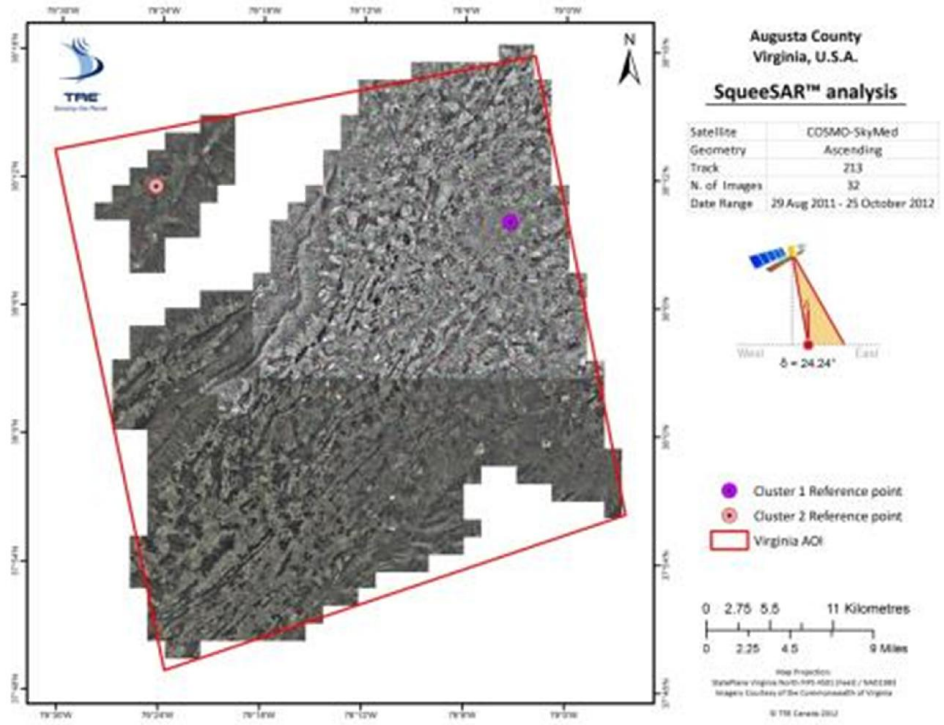

Figure 6 - Location of the two data clusters and respective reference points.

The large size of the AOI and the large swatch of densely vegetated terrain running through the northwest corner necessitated the processing of the image stack as two separated clusters: the larger one corresponding to **cluster 1** and the smaller one in the northwest corner to **cluster 2** (Figure 6)**.**

Reference point

Both permanent and distributed scatterers where identified throughout the AOI. Buildings, roads, fences and other man-made structures provide the basis for many PS points in the SqueeSAR analysis. Many natural features such as rocks or exposed ground were also likely sources of stable PS targets.

DSs correspond to large areas (up to hundreds of square meters) and were identified from exposed areas such as bare ground or fallow fields. It is important to consider that while DSs are represented as individual points for clarity of presentation and ease of interpretation, these measurements actually correspond to non-point features that are multiple pixels in size. The size of the DSs within the AOI ranges from 76 to 891 m^2.

SqueeSAR is a differential technique meaning displacement is measured compared to a reference point that is assumed to be stable. The reference points used for the two clusters are both shown in Figure 6. The reference points were selected using an optimization procedure that performs a statistical analysis of all targets to select a point with optimal radar parameters (including high coherence, low standard deviation and low temporal variability). The use of this procedure ensures the highest quality results are achieved.

Table 3 provides the localization of the reference points for the two clusters as well as a summary of the processed data properties.

Table 3 - Statistics of processed data.

Satellite	COSMO-SkyMed (CSK)
Acquisition geometry	Ascending
Analysis time interval	29 August 2011 - 25 October 2012
Number of scenes processed	32
Georeferencing	PS aligned on orthophotos (1 foot resolution)
Projection system used / datum	State Plane Virginia North FIPS 4501 (Feet) / NAD 1983
Reference Point location (Cluster 1)	6744485.69 N; 11323234.49 E
Reference Point location (Cluster 2)	6754696.17 N; 11222525.69 E
Area of interest	617.8 sq. mile (1,600 km^2)
Number of PS + DS (Cluster 1) **Number of PS** **Number of DS**	296,121 166,348 129,773
Number of PS + DS (Cluster 2) **Number of PS** **Number of DS**	2,695 1,453 1,512
Average PS + DS density (Overall)	484 PS and DS/sq. mile 187 (PS and DS/km^2)

Each PS and DS have an associate measurement error expresses as standard deviation values of the displacements. This is affected by several factors:

- Spatial density of the PS and DS (higher density produces higher precision)
- Quality of the radar targets (higher signal-to-noise ratio produces higher precision)
- Distance from the reference point (the closer the higher the precision)
- Number of images processed (the higher the number the higher the potential precision)
- Period of time covered by the imagery (longer time might provide better tracking of the ground deformation)
- Climatic condition at the time of the acquisition (water vapor is the main source of phase noise from the atmosphere)

In addition to each measurement point having an associated standard deviation value to represent the error of the displacement measured, results can also be characterized by the accuracy of the technique. Specifically, three parameters are used to characterize the overall accuracy of the results:

- Precision of the estimated deformation rates
- Precision of the estimated elevations
- Precision of the geocoding

Displacement rate

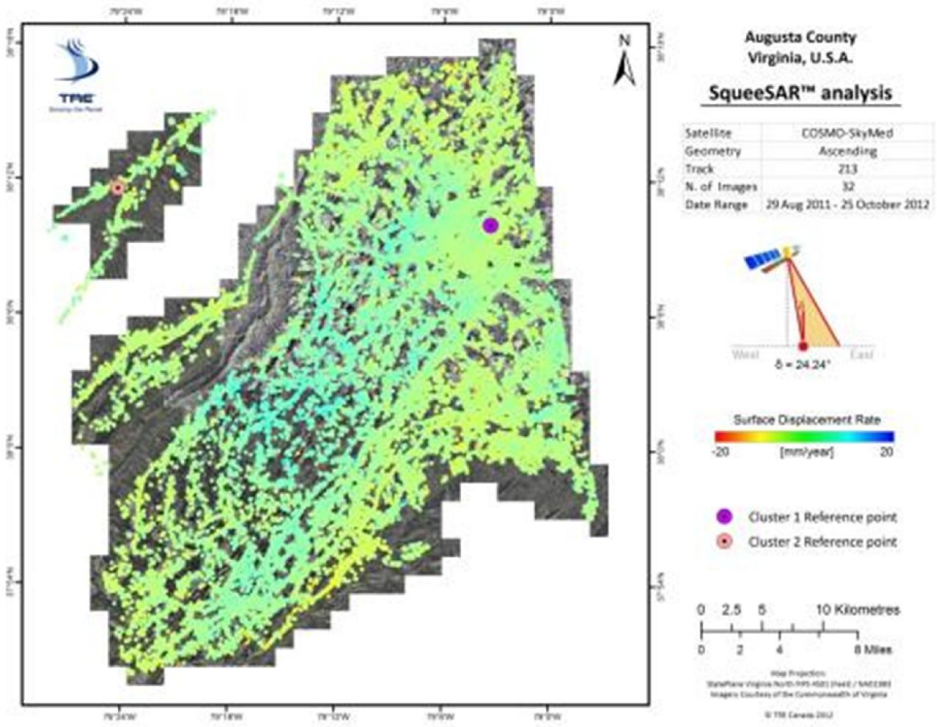

Figure 7 - PS and DS deformation rates in mm/year.

The line-of-sight (LOS) displacement rates, expressed in mm/year, as detected from the processing of all images are shown in Figure 7. Each point corresponds to a Permanent Scatterer (PS) or a Distributed Scatterer (DS), and is color-coded according to its annual rate of movement. Average displacement values are calculated from a linear regression of the ground movement measured over the entire period covered by the satellite images. Detailed information on ground motion is also provided by means of displacement time series, which were provided for each PS and DS.

Displacement rates are fairly stable over the entire AOI. Results identified within the middle of the area show mild uplift, which may be related to seasonal influences such as changes in temperature or ground water levels. Many areas of localized displacement can be observed in the results when viewed on finer spatial scale.

Displacement standard deviation

The standard deviation of the surface displacement data characterizes the error of the measurement (Figure 8). The displacement rate for a given point should be read in the form of *displacement rate* ± *standard deviation*. Areas impacted by higher standard deviation indicate a greater variability in measured displacement, and are helpful in identifying surface features with inconsistent movement patterns.

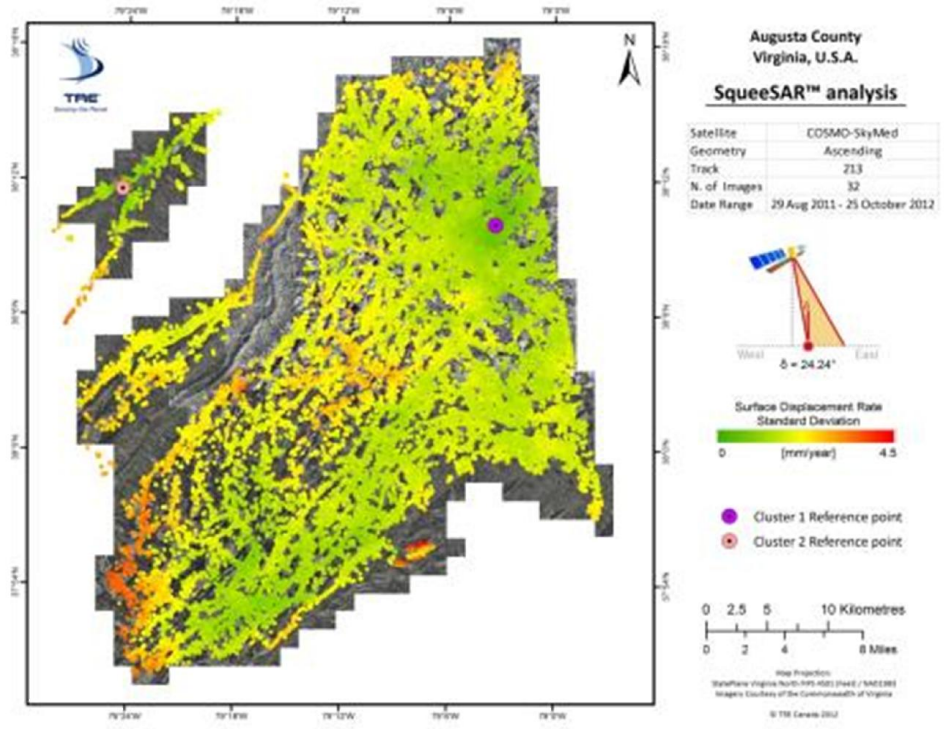

Figure 8 - Standard deviation of the deformation rates.

The average standard deviation values associated with the measured displacement rates is 1.5 and 1.4 mm/year for points within cluster 1 and cluster 2 respectively. As a comparison, consider the values that were obtained after the processing of the first year data: 3.38 and 8.67 mm/year respectively. This is in line with the discussed property of the SqueeSAR algorithm that provides higher confidence levels of the measurement points when a larger number of images over a longer period are available for processing. Measurement precision typically reaches the millimeter scale once at least 12 to 18 months of images are acquired. Areas furthest away from the reference point and/or with a lower density of identified points tend to exhibit slightly higher standard deviation values.

Acceleration

PS and DS acceleration values (Figure 9) can be used to identify non-linear trends in the deformation time series. Acceleration is used to identify areas where the deformation rate is increasing or decreasing over time. Negative accelerations are marked in red and indicate either an increase in downward movement rates, or a decrease in uplift. Positive accelerations are blue and indicate either an increase in the rate of uplift or a decrease in the rate of subsidence.

The range of acceleration rates measured over this area has decreased by more than half compared with the results obtained after processing the first year of data.

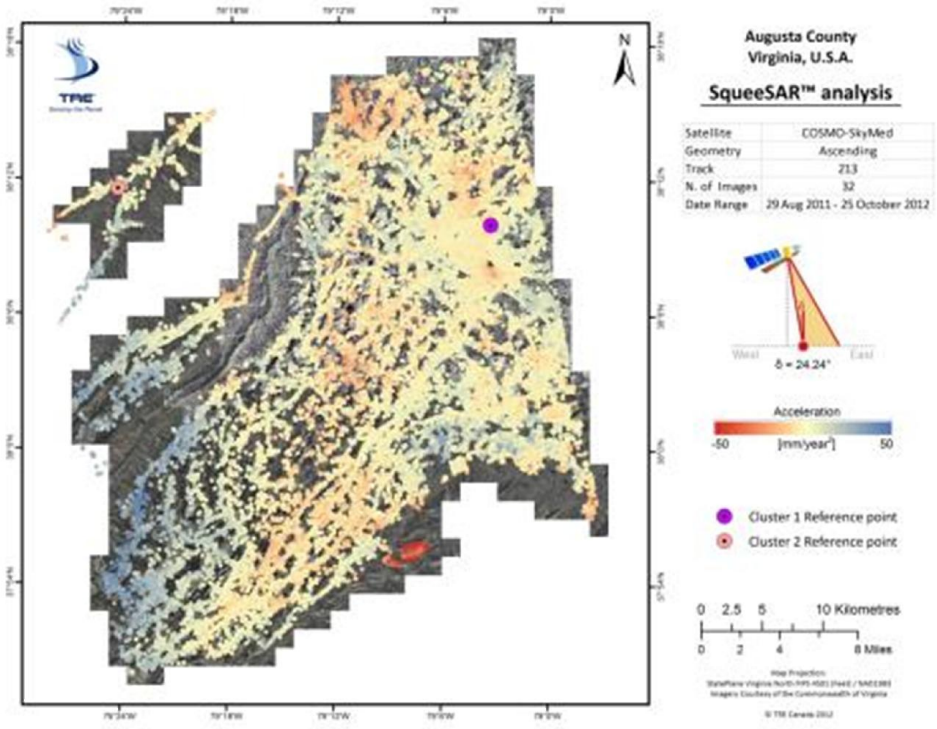

Figure 9 - PS and DS acceleration values expressed in mm/year^2.

Both positive and negative acceleration values were identified throughout the AOI, with most of the western side exhibiting positive acceleration (corresponding to a decrease in the rate of subsidence), whereas most of the remaining area demonstrated either stable values or mild negative acceleration rates (indicating a decrease in the rate of uplift). It is expected that these values are related to changes in seasonal movement patterns over time in this area (i.e. uplift during the winter months, followed by subsidence during the summer months).

Acceleration standard deviation

The precision of the acceleration data (one standard deviation) is shown in Figure 10. The acceleration rate for a given point should be read in the form of *acceleration* ± *standard deviation*. Standard deviation values of the estimated acceleration values can also be used to identify areas of highly variable movement.

Standard deviation values associated with estimated acceleration have also decreased with respect from the previous processing. The average acceleration standard deviation is 9.6 and 8.7 mm/year^2 for cluster 1 and cluster 2 respectively. The distribution of acceleration standard deviation values is similar to the displacement rate standard deviation values.

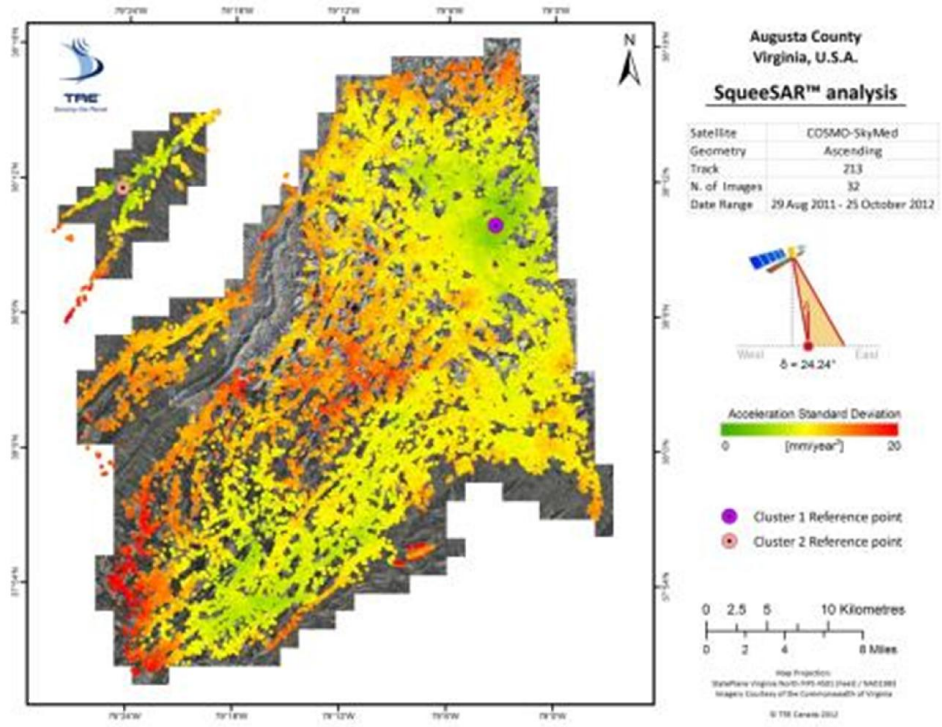

Figure 10 - Standard deviation of the acceleration values, in mm/year^2.

Cost-benefit analysis

Introduction

As one of the project objectives VDOT performed a Cost-Benefit Analysis (CBA) to determine the longer term viability of using remote sensing techniques such as InSAR. The CBA is a systematic procedure to determine the economic viability of a project by comparing the total expected benefits against the total expected costs.

Benefits and costs are expressed in monetary terms and adjusted using an interest rate (or a discount rate) to take into consideration the time duration factor. Cash flows, considered as either benefits or costs, might occur at different times during the project and must be converted to a common reference. In this analysis we used the Annual Worth (AW) method: all cash flows are converted to their AW equivalencies. The conversion value is calculated as the payment for a loan based on constant payments and a constant interest rate.

Once the benefits and costs are converted to AW, the final ratio B/C can be evaluated: the project is considered economically viable if $B/C \geq 1$. For values close to unity, other non-economic factors may need consideration to reach the final decision.

In this study we used the following relation:

$$\frac{B}{C} = \frac{AW_{benefits}}{AW_{intial\ investment} - AW_{savage\ value} + AW_{M\&O}}$$

Salvage value, when an estimate is available, is considered a positive cash flow (subtracted from the initial investment) whereas the annual maintenance and operation costs ($AW_{M\&O}$) are considered a negative cash flow (therefore included with the costs).

A **discount rate of 7%** and a **service life of 20 years** were assumed.

Estimation of benefits

In this analysis the benefits were derived indirectly from the estimated cost saving provided by the implementation of the proposed InSAR technology.

Sinkholes and landslide remediation is currently done mostly on an emergency basis. Immediate action after an incident occurred is required due to the considerable safety issue and to reduce the exposure of DOTs to legal liability. The direct benefit that early detection provides is the ability for DOTs to plan the maintenance thus obtaining better rates from subcontractors (providing substantial cost saving) and minimizing disruption to services.

The estimated annual saving was computed according to the following model:

$$E_s = (\eta_e - \eta_{ne}) \cdot \mu_{hrs} \cdot n_{yr} \cdot \eta_{det}$$

where:

E_s is the *estimated annual saving*

η_e is the *emergency repair rate (on a per-hour basis)*

η_{ne} is the *non-emergency repair rate (on a per-hour basis)*

μ_{hrs} is the *average number of hours required to fix an incident*

n_{yr} is the *number of incidents per year*

η_{det} is the *incident detection rate*[1]

This model currently assumes that repair works, whether emergency or non-emergency, cause the same level of economic loss in terms of highway closures and disruptions to commerce, and that the hourly costs for repairing sinkholes, restoring landslides and bridge settlements are weighted to reach an average hourly repair rate.

An estimate of the variables used in the model can be inferred from historical data involving repair works by a DOT.

Since the estimated benefits in terms of annual savings start from Year 3, a benefit adjustment for Year 2 is computed. Noting that by convention in a cost-benefit analysis all costs are considered positive, the equivalent AW is added to the estimated annual savings to arrive at the total annual benefits.

Estimation of costs

The total AW of estimated costs is derived from two major components:

- project related expenditures over the two-year project period
- estimated annual costs starting from Year 3

Project expenditures

The project expenditures include initial capital investment and InSAR imagery acquisition costs distributed over two years. The values are obtained directly from the *Technical and Deliverable Milestone Schedule* (Attachment 3 to the Cooperative Agreement #RITARS-11-H-UVA. The values for Year 2 are converted to their Present Worth (PW) by application of the discount rate followed by the AW equivalency calculation.

Estimated annual costs

The estimated annual costs are mainly composed of:

- InSAR imagery acquisition cost
- Maintenance and Operation cost
- Cost due to false positive detections

[1] The *incident detection rate* will be determined from the validation study of the InSAR detection techniques.

Among the three, the imagery acquisition cost contributes the most and may have a significant impact on the project's economic feasibility. It is computed as follows:

$$I_{cost} = P_{cost} \cdot n_p \cdot n_s \cdot f_s$$

where:

I_{cost} is the *imagery acquisition cost*

P_{cost} is the *price for one SAR image (swath).* In this analysis it refers to the price per swath (obtained from satellite sensor arrays) after TRE processing. It was obtained by dividing the total cost charged by TRE by 16 (only one swath is required to cover the AOI and there are 16 swaths in a stack).

n_p is the *number of swaths required to cover the AOI*

n_s is the *number of temporal acquisitions needed to process data to the required accuracy and provide the final product*

f_s is the *yearly frequency at which final products are required by the customer*

Clearly, the cost of imagery acquisition grows quickly with the size of the AOI, the data accuracy requirement, as well as the final product delivery frequency: a larger AOI and a more precise displacement history will require more images thus increasing costs.

The annual M&O cost includes those involving software update, hardware upgrade, and personnel, etc., and is not anticipated having a significant impact on the B/C ratio.

The cost of false positive detections accounts for the expenses incurred due to the dispatch of ground validation teams to location erroneously detected by the proposed methodology that turn out not to be of concern. It may be greatly reduced by including historical and geological data within the detection algorithm.

Any salvage value (for example the software value) was first converted to its present value, and then to its AW equivalent, which was subtracted from costs as an adjustment for Year Two in the estimation of total annual costs.

Results

Shown in Figure 11 and Figure 12 are the B/C ratio versus incident detection rate (η_{det}) and number of temporal acquisitions (InSAR images per stack) (n_s), respectively, at a discount rate of 7% and a service life of 20 years.

Only one variable is changed at a time with all others kept constant. In particular, the incident detection rate is varied from 40% to 100% in Figure 11, with the number of InSAR images per stack kept at 16, and all other variables kept constant.

In Figure 12 the detection rate is kept at 80% whereas the number of InSAR images per stack is varied from 2 to 32 (TRE is scheduled to deliver 2 stacks with 16 images per each over the project period of two years).

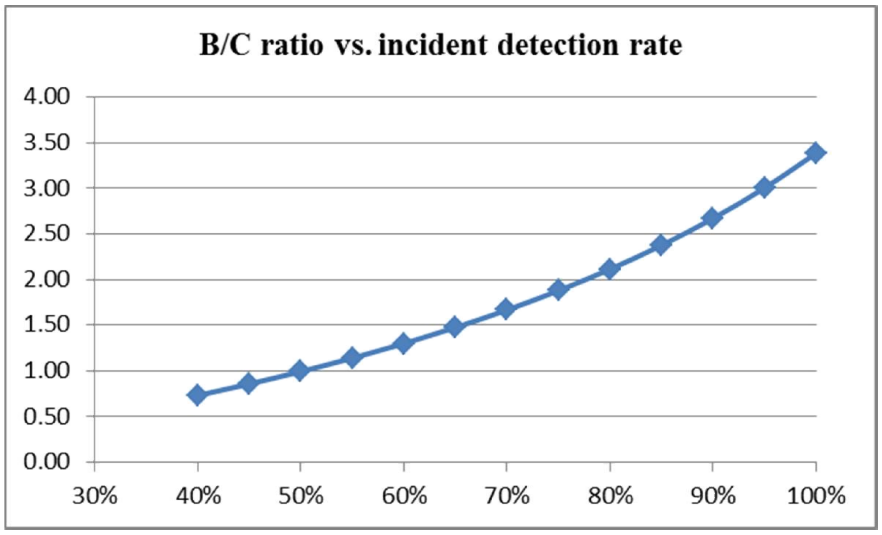

Figure 11 - B/C ratio vs. incident detection rate at an InSAR imagery acquisition frequency of 16/yr

It can be seen that **a detection rate greater than 50% justifies the economic feasibility of the project**. At this detection rate, the imagery acquisition frequency does not directly impact the economic feasibility of the project but will reduce the B/C margin.

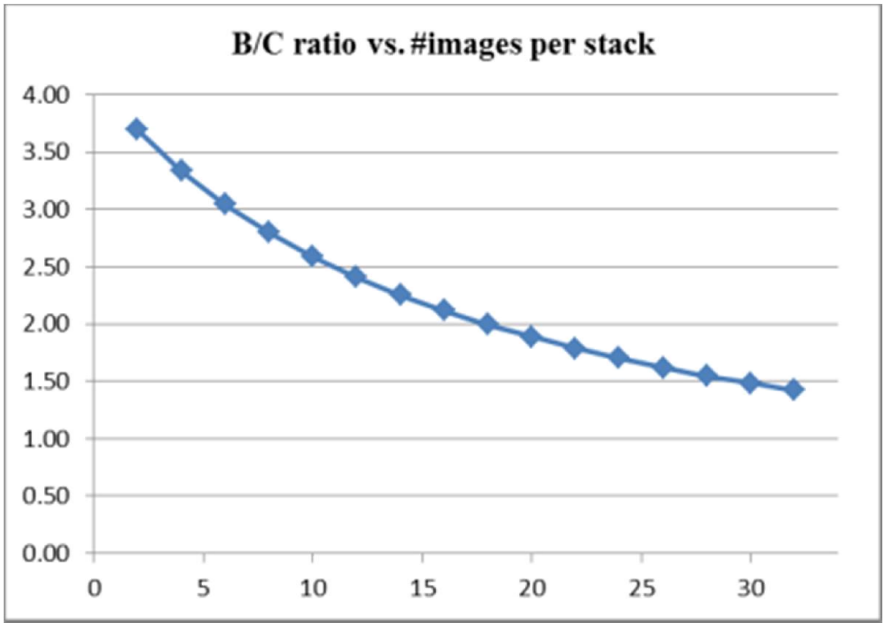

Figure 12 - B/C ratio vs. number of InSAR images per stack, at an incident detection rate of 80%

Comments

The size of the area of interest has a significant impact on InSAR imagery acquisition costs. If the DOTs are interested in large area or state wide coverage coverage, TRE is now able to estimate the long term running costs of imagery acquisition of extensive regions. We note that these data acquisition costs will change dramatically (becoming lower) as new sources of input radar data become available. These new sources include ESA Sentinel, RCM Constellation, and SAOCOM all of whose policy mandates will

ensure raw data becomes available at no cost. (Note that the entire cost of obtaining deformation changes from InSAR will not become zero due to processing costs that will remain even if the raw data approaches zero cost.)

To further reduce cost, a DOT may consider cost-sharing with other public agencies or private sector businesses that may be interested in the service capabilities related to InSAR analysis. For example, DOTs may only be interested in detecting impending sinkholes and landslides within the road system under their jurisdiction, while those elsewhere may be of significant interest to land developers.

The current model used to estimate annual savings may be improved to reflect the differences in incident types, road types, as well as in rates taking into account the time periods over which the repair work is performed, e.g., nightly and daily rates.

Manual data analysis

The results presented in this section represent more than one year of surface displacement monitoring over the AOI. Many areas of highly localized movement were detected, several of which warranted closer inspection of the time series (detailed in the following subsections). Due to the analysis of a larger data stack collected over a longer period of time, the precision of the results has increased and movement trends are better characterized at this site as compared with the interim results presented during the project.

A band of mild uplift in the center of the AOI was the only regional deformation trend identified. This pattern may be related to the cyclical movement caused by seasonal effects, such as changes in soil moisture/ground water or temperature fluctuations, or other environmental factors. Seasonal trends tend to have a larger impact on the deformation rates of data stacks collected over shorter time spans, but become more accurately characterized once several years of imagery are collected.

The large number of points identified from this analysis allowed for the detailed characterization of movements within many parts of the AOI, especially over urban areas and other man-made infrastructures. Particular attention was given to smaller zones of subsidence located close to areas of interest which may be related to geological instabilities. A brief inspection of the InSAR data in relation to regional terrain characteristics and geology was also undertaken.

Comparison to geohazard event data

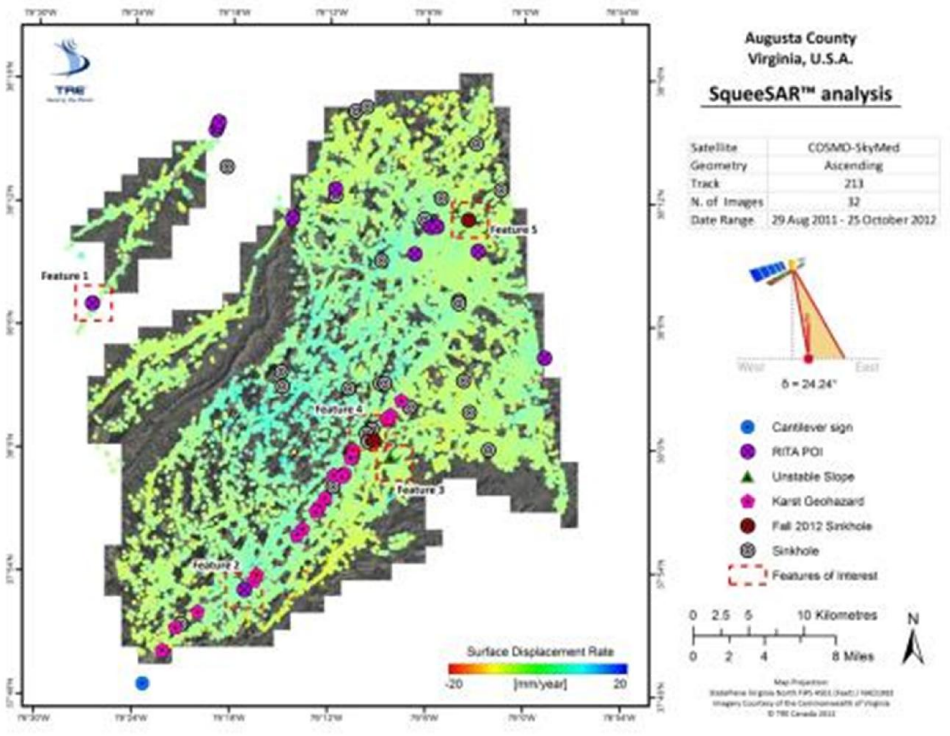

Figure 13 - Historic geohazard event data and points of interest within the AOI overlaid on the displacement results.

Figure 13 - Historic geohazard event data and points of interest within the AOI overlaid on the displacement results. shows historic sinkholes, landslides and other geohazard data provided by VCTIR overlaid with the displacement rates results obtained by TRE. A total of 30 sinkholes, as well as one slope failure are located within the AOI. The locations of 23 karst geohazards located along interstate 81 are also available as well as an additional 15 points of interest indicating features that may be of interest to the transportation infrastructure (specifically in relation to the detection of sinkholes, landslides and road/bridge monitoring).

Global regional analysis

Primary road network

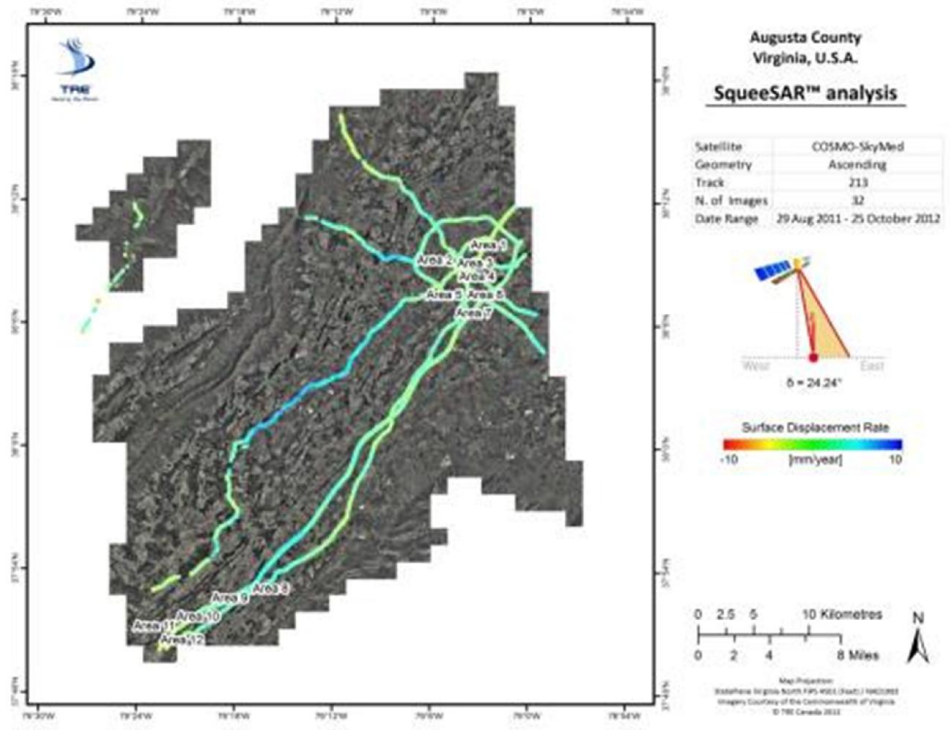

Figure 14 - Surface displacement results identified within a 30 m (100 foot) buffer of major roads within the AOI. Twelve subsiding roads are indicated and their information listed in Table 4.

There is an interest in identifying any subsidence detected on, or in close proximity to any major road within the AOI. A focused inspection of the data was therefore carried out to isolate and highlight any movement occurring within 30 meters (100 feet) buffer around eight primary roads (I-81, I-64, Rt.11, Rt.250, Rt.254, Rt.262, Rt.252, and Rt.600).

Twelve sections of road are identified in Figure 14 which only shows displacement rates for measurement points identified within this 30 meters buffer. The specific locations of permanent scatterers indicating subsidence in these twelve areas are listed in Table 4.

Two of these areas were selected for further inspection and are analyzed in detail in the following subsections as they provide interesting examples of how InSAR data can be

used to identify movement over highly localized areas. All of these measurement points are point scatterers and are labeled 'TS' to indicate "Time Series".

Table 4 - Coordinates of the twelve subsiding major roads identified in Figure 14. All coordinates were obtained from permanent scatterers. Area 10 represents the center of a large linear group of subsiding measurement points.

Area	Location	Description
1	38°9'58.8" N; 79°2'35.7"W	Railroad track running parallel to Lee Highway (Rt. 11)
2	38°9'19.6" N; 79°5'54.3"W	West Beverley Street (Rt. 254)
3	38°8'49.2" N; 79°4'7.7"W	Railway track overpass above Lee Highway (Rt. 11)
4	38°8'31.1" N; 79°3'10.9"W 38°8'30.4" N; 79°3'10.8"W	Richmond Avenue (Rt. 250)
5	38°7'35.4" N; 79°5'12.6"W	Exposed ground on the shoulder Woodrow Wilson Parkway (Rt. 262)
6	38°7'27.1" N; 79°2'40.5"W	Off-ramp from I-81
7	38°6'44.6" N; 79°3'24.6"W 38°6'43.9" N; 79°3'24.4"W	State Route 635 bridge overpass above I-81
8	37°53'15.5" N; 79°16'50.0"W	Exposed ground on the shoulder of I-64
9	37°52'35.7" N; 79°18'17.6"W	Construction along shoulder of I-64
10	37°51'52.0" N; 79°20'14.5"W	Construction along shoulder of I-64
11	37°51'8.6" N; 79°21'28.2"W	Construction along shoulder of I-64
12	37°50'44.2" N; 79°21'11.8"W 37°50'43.3" N; 79°21'13.8"W	Apparent rip-rap slope along shoulder of Rt. 11

Area 4 – Richmond Avenue (Rt. 250)

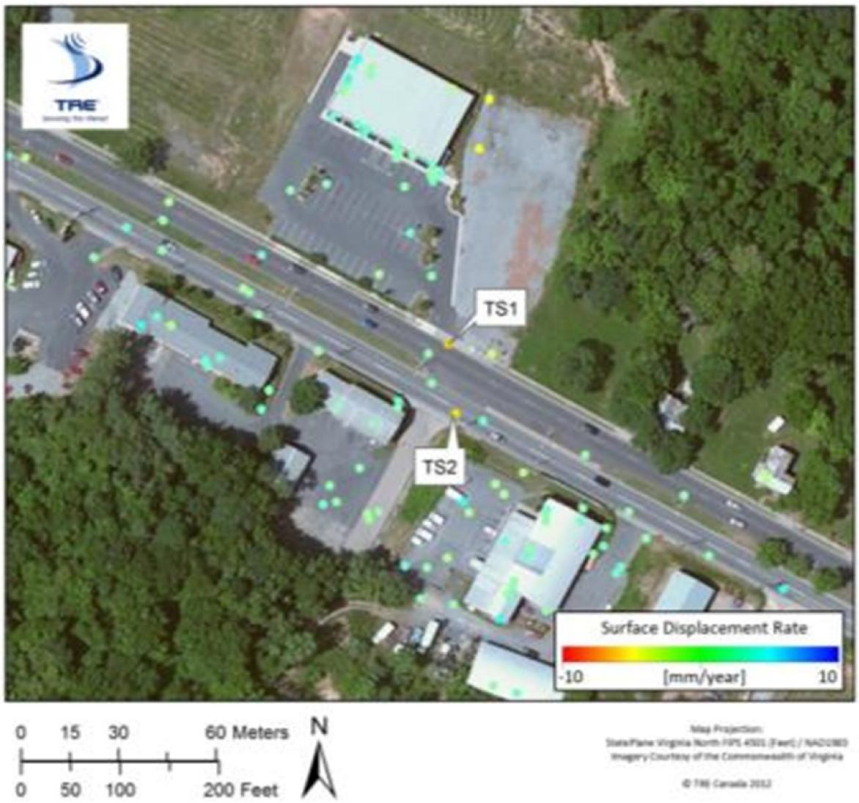

Figure 15 - A close-up of displacement results over a portion of the Virginia AOI designated as Area 4 in Figure 14.

Two points indicating mild subsidence were highlighted in area 4 which is locate on a portion of Richmond Avenue (Rt. 250) (Figure 15). Time series for these two points are shown in Figure 16 and Figure 17. A slight drop in the ground surface was observed at the end of June 2012 in both of the time series of these measurement points. Subsequent field inspection indicated that TS1 and TS2 points correspond to newly installed steel posts supporting overhead traffic signs.

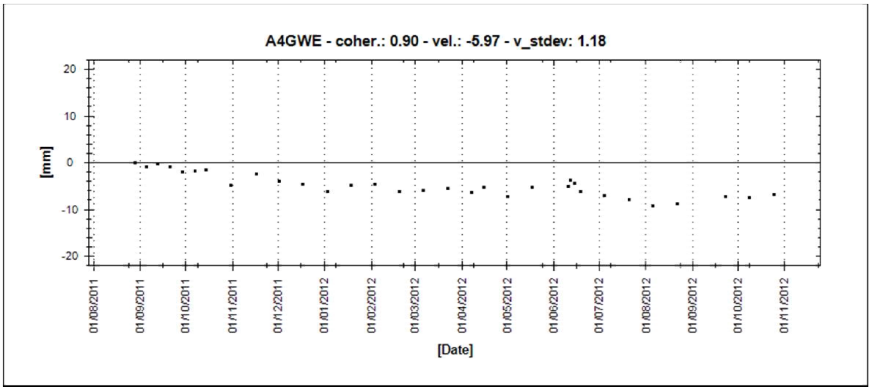

Figure 16 - Time series of surface displacement for the measurement point identified as TS1 in Figure 15.

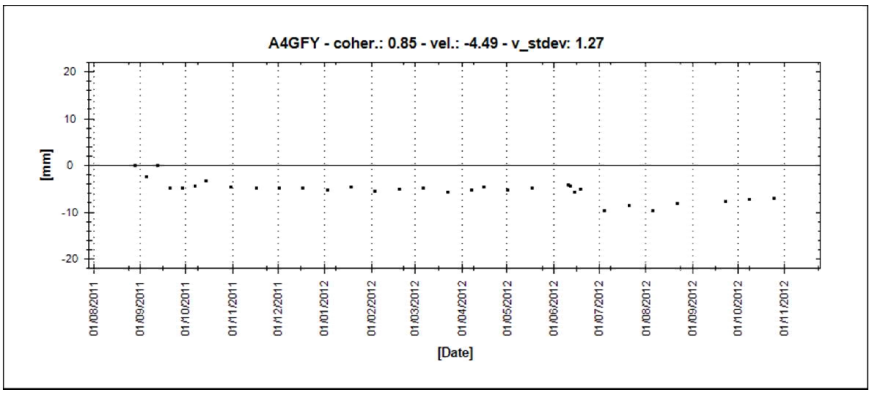

Figure 17 - Time series of surface displacement for the measurement point identified as TS2 in Figure 24.

Area 6 – Shoulder off I-81 ramp

Figure 18 - A close-up of displacement results over a portion of the Virginia AOI designated as Area 6 in Figure 23.

Two measurement points identified on the shoulder of an off-ramp from I-81 were identified in area 6 (Figure 18). An average time series of these two measurement points show a drop in mid-April 2012. Subsequent field inspection indicated moderate surface erosion. This location corresponds to a culvert running under the roadway and discharging at the embankment slope.

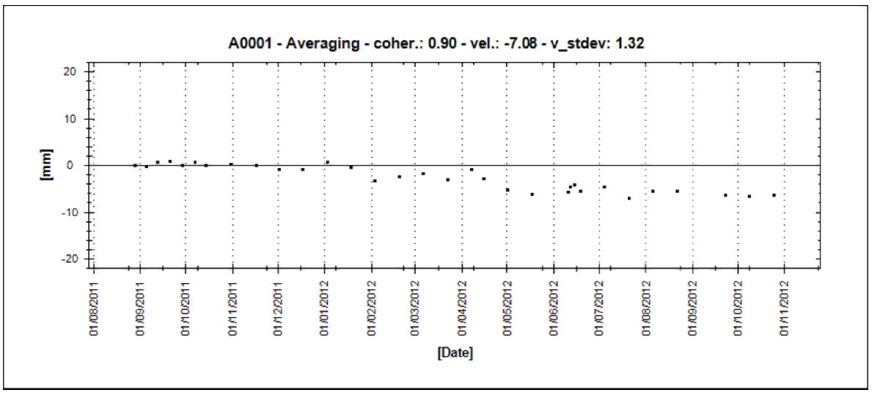

Figure 19 - Average time series of surface displacement for the measurement point identified in Figure 18.

Slope analysis

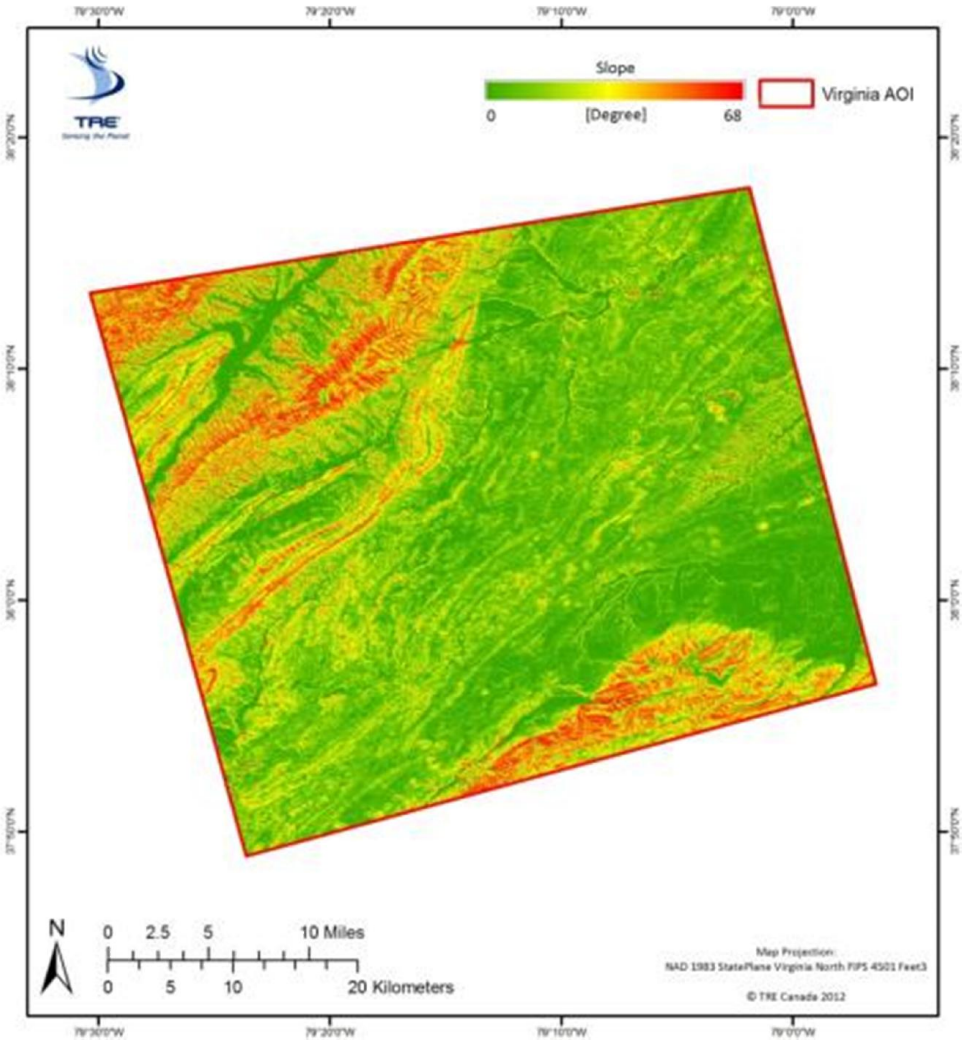

Figure 20 - An overview of the slope values calculated from the DEM obtained over the AOI.

There is interest in investigating whether any correlation between slope angle and displacement rate could be identified. In order to perform this comparison, slope

gradients were calculated using the Spatial Analysis package of ArcGIS and a digital elevation model (DEM) acquired through the National Elevation Dataset (NED). The DEM was created by the U.S. Geological Survey (USGS) at a resolution of 1/3 arc-second (approximately 10 meters) within a time range between 1999 and 2009.

The slope, expressed in degrees, denotes the steepness between two particular points, where higher slopes indicate steeper terrain. Figure 20 shows an overview slope map for the AOI. Slope values calculated over the AOI range from 0° to 68°, with the steepest slopes located in the mountainous areas in the northwest and southeast of the AOI.

In order to explore any possible relationship between ground deformation and slope, the SqueeSAR data was divided into four groups based on the slope measurement (Table 5). Average displacement rates calculated within each of these four slope categories were determined; however, no consistent trend was identified between ground deformation and slope over the AOI. Due to the high density of SqueeSAR measurement points identified from urban areas, more than 95% of the data was located in a region with slope less than 10°.

Table 5 - A summary of average displacement rates for the four slope classes.

Slope Class (degree)	Proportion of SqueeSAR data	Average displacement rate (mm/year)
0-10	95.12%	0.20
10-20	4.21%	0.08
20-30	0.44%	-0.40
>30	0.23%	-0.28

Figure 21 to Figure 24 show the average time series for all measurement points identified within the four different slope classes. For the results identified on slopes greater than 20°, the average displacement rate changed from uplifting (positive) to subsiding (negative). The average time series for the two steeper slope classes (Figure 23 and Figure 24) have a cyclical pattern, with subsidence observed over the first six months of the analysis followed by a period of uplift during the second half of the monitoring period. This trend may suggest that seasonal displacement is more evident over areas with steeper slopes; however it may also be a result of the small proportion of the data used to create these average time series. Further comparison between the displacement data and slope gradient is necessary to accurately identify any possible correlation.

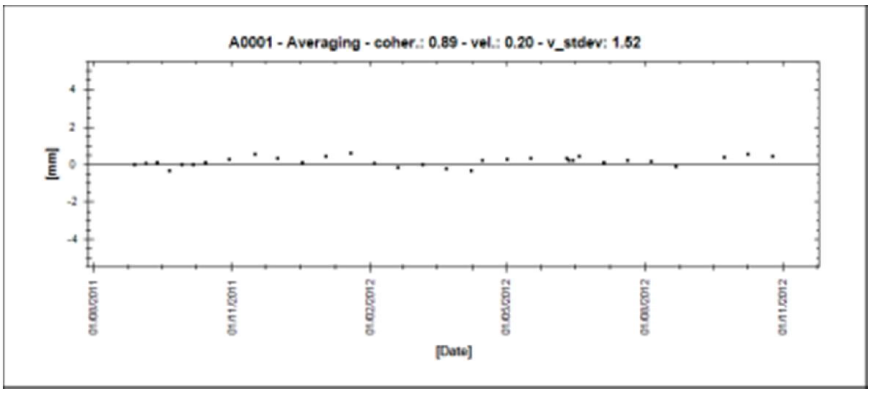

Figure 21 - Average time series of surface displacement for data points with a slope of 0° to 10°.

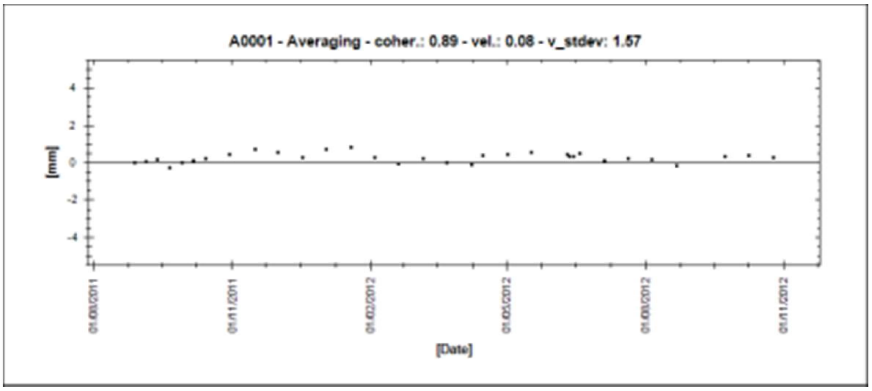

Figure 22 - Average time series of surface displacement for data points with a slope of 10° to 20°.

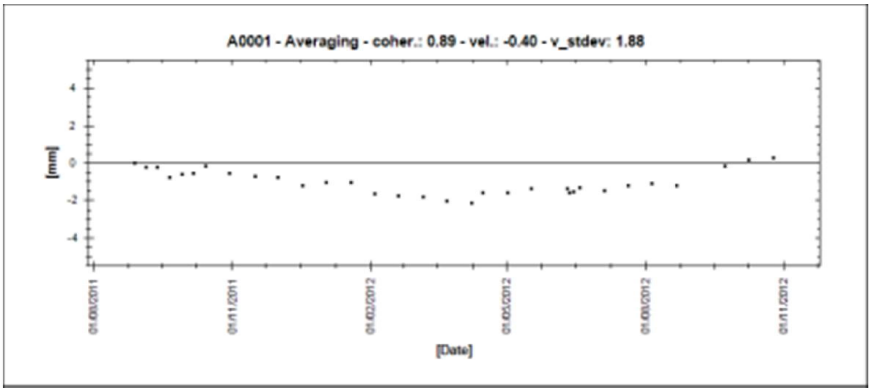

Figure 23 - Average time series of surface displacement for data points with a slope of 20° to 30°.

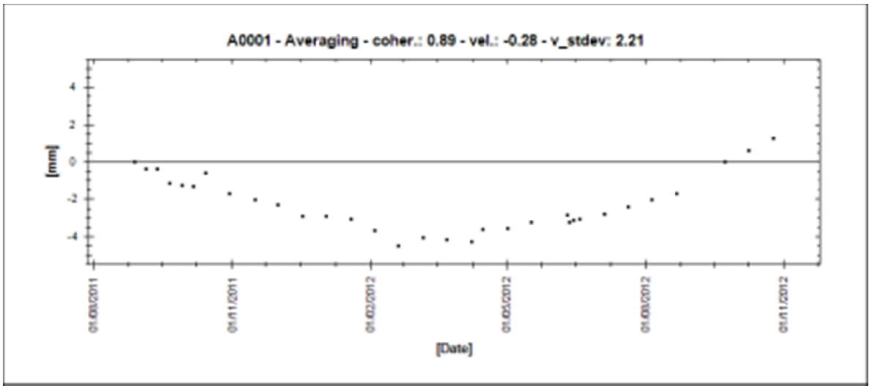

Figure 24 - Average time series of surface displacement for data points with a slope greater than 30°.

Geological features correlation

The SqueeSAR data was also integrated with geological data to determine whether any general correlation could be observed between surface displacement and location geology. Geology data was acquired from the USGS and was separated into 5 classes listed in Table 6.

Table 6 - Categories of geological data identified within the AOI.

	Geologic data category
1	Elbrook Formation (Cambrian)
2	Conococheague Formation (Cambrian-Ordovician)
3	Beekmantown Group (Ordovician)
4	Edinburg Formation Lincolnshire and New Market Limestones (Ordovician)
5	Other

Figure 25 shows the average time series detected for all measurement points identified within each geologic category. No strong relation between the overall surface deformation and any of the geologic data categories was observer; however, these result demonstrated that measured surface deformation varied the most under the miscellaneous "Other" category. More detailed analyses are required to further investigate the presence of any trends in the displacement results with respect to geology.

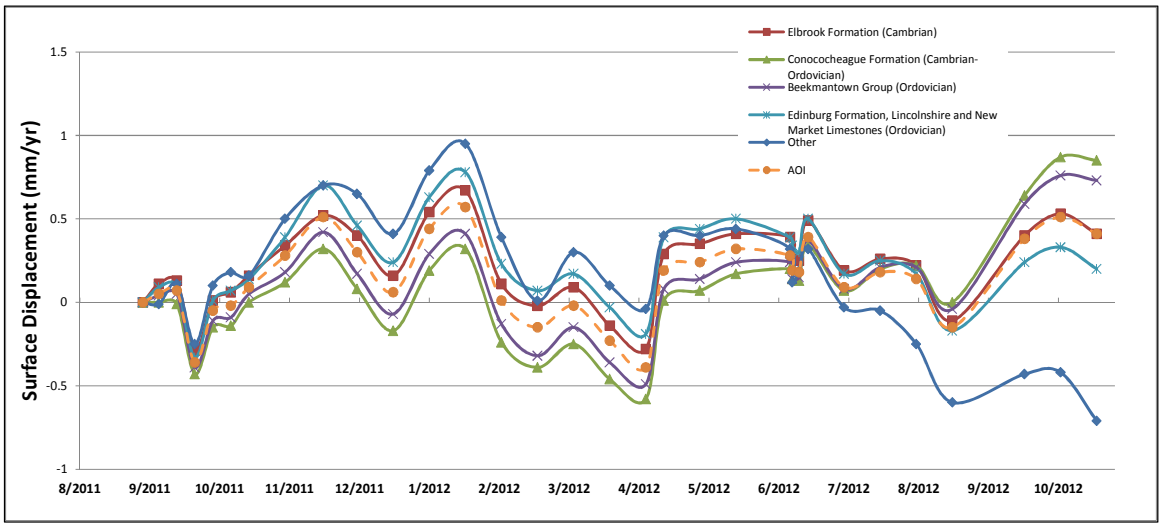

Figure 25 - Average time series according to geologic category.

Automated image analysis

In the previous sections we presented results on how the analysis of permanent, distributed and temporary scatterer can provide an effective set of tools to analyze and monitor features of interest to the transportation community. The tools are based on user intervention for the definition of the analysis region. In the following section we present algorithms that were developed to automate detection and analysis of features, with particular emphasis to the detection of sinkholes. These methods, in particular the feature tracking, were designed to be easily extensible to detect/analyze other features.

We pursued two main approaches to detection of geohazards, a graph theoretic approach and a parametric approach. In the graph theoretic approach, an optimization problem is solved that essentially "cuts" through the images, separating hazardous regions from non-hazardous regions [6]. This approach does not exploit the evolution of features over time. In the parametric approach, we attempt to fit parametric models to spatiotemporal, multidimensional data [7]. Such an approach can discover trends in time and space that are consistent with certain geophysical or structural phenomena.

Graph theoretic approach

Method

A graph cut is a segmentation technique for an arbitrary graph via the cutting of edges. The optimal cut is one which has minimum energy given by

$$E_{cut} = \sum_{u \in A, v \in B} w(u, v) \tag{1}$$

where A and B are the disjoint sets of vertices created by the cut, and $w(u, v)$ is the weight of a given edge between vertices (u, v). Typically the energy of a cut is expanded to include a measure of the association between 'cut' sets [8] A and B – this promotes spatial coherence preventing small, isolated vertices from being unnecessarily cut away.

This expansion is sometimes termed the *normalized cut*:

$$NE_{cut} = \frac{E_{cut}(A, B)}{assoc(A, V)} + \frac{E_{cut}(A, B)}{assoc(B, V)} \tag{2}$$

and

$$assoc(A, V) = \sum_{u \in A, t \in V} w(u, t) \tag{3}$$

$$assoc(B, V) = \sum_{u \in B, t \in V} w(u, t) \tag{4}$$

In (3) and (4) t is any other vertex in the set of all vertices V. An alternative cut expression to (2) is provided in [9]:

$$E_{cut}(f) = \lambda \sum_{p \in P} R_p(f_p) + \sum_{\{p,q\} \in N} B_{\{p,q\}}(f_p, f_q) \quad (5)$$

where p and q are vertices, B is the associative term, R is the traditional energy assigned to an edge, and λ is a weighting factor.

To extend this approach to the automated detection of features within the dataset provided by TRE we must first construct a graph from a pointcloud data set. The points are takes as vertices of the graph while edges are created applying a Delaunay triangulation [10]. The Delaunay triangulation (in two dimensions) ensures that the cricumcircle of each triangle created has an empty interior, thus this triangulation scheme maximizes the minimum angle of each triangle produces and creates non overlapping edges, resulting in an edge construct that accurately reflects local neighborhood relationships.

Our data set is unique since it offers multiple facets of information for each scatterer: displacement time series, coherence, velocity, acceleration, physical area represented (for distributed scatterer), elevation, location, etc. So the feature data set is broadened, as are the factors which might be used to characterize the edge weights. Between the available factors, we selected those that might most immediately and accurately indicate the presence of a sinkhole forming region:

- Relative displacement between two vertices
- Displacement range
- Coherence

We chose to use displacement difference in place of the slope of displacement in order to separately consider and independently weight the length of an edge.

As previously described, the graph cut approach requires the definition of the cost associated with the cutting of an edge. To obtain this cost function, we started by defining energies associated with the identified factors. These energies were explicitly defined to minimize the cost of cutting an edge at the boundary of a region of possible sinkhole formation:

- Large displacement between two vertices
- Displacement magnitude which resides within a narrow, sufficiently negative band of displacements

For each edge e_i connecting vertices (v_{i_1}, v_{i_2}) with displacement (d_{i_1}, d_{i_2}), average displacement d_{avg} and average coherence coh_{avg}, we defined the following energies:

$$E_{band}(v_{i_1}, v_{i_2}) = \begin{cases} 0 & \text{if } d_{low} < d_{avg} < d_{high} \\ min(|d_{high} - d_{avg}|, |d_{low} - d_{avg}|) & else \end{cases} \quad (6)$$

$$E_{diff} = \frac{1}{|d_{i_2} - d_{i_1}|} \quad (7)$$

$$E_{reliable} = \frac{1}{coh_{avg}} \tag{8}$$

$$E_{length} = length(e_i) \tag{9}$$

where $d_{high} = \max(d_{i_1}, d_{i_2})$, $d_{low} = \min(d_{i_1}, d_{i_2})$, $d_{avg} = (d_{i_1} + d_{i_2})/2$. E_{length} was included to give priority to cuts that pass through shorter (thus more accurate) edges in turn increasing the overall accuracy of the cut.

In order to facilitate a meaningful combination of these energies, each was normalized to the same means and standard deviation resulting in the final energy function:

$$E = \alpha \cdot E_{band} + \beta \cdot E_{diff} + \gamma \cdot E_{reliable} + \delta \cdot E_{length} \tag{10}$$

where α, β, γ, and δ are inter-category weighting parameters.

We omit any associativity parameters in the composite energy function, as we do not wish to explicitly encourage spatial coherence. In fact, some points in the dataset may represent physical areas which are actually quite large. If such a point has associated data and trends with surrounding pixels accurately indicating that a sinkhole may be forming, the algorithm should not discourage a cut around that point and in the process miss a segmentation of a potential sinkhole-forming region.

Once this conglomerate energy function is achieved, we then find minimum-energy graph cuts. The number of cut contours is determined by the number of statistically significant energy minima present after each cut. Lastly, we fit a spline to these cuts, using the midpoint of each edge as interpolant points—these splines are the final result of the segmentation.

Data set

We started by analyzing the spatial changes in the profiles of known sinkholes. This area of study resides close to Wink, Texas, occupies about 55km^2, and is imaged in one of the test data set provided by TRE: a sparse, non-uniformly sampled point cloud (93,513 points between PSs and DSs) derived from 22 InSAR images acquired over a period of about 69 months between June 1992 and February 1998 by the European Remote-Sensing (ERS) satellites. The sinkholes present in this area are likely the result of upward migrating cover-collapse solution cavities due to drilling in the 1920s [11]: one (Wink 1) collapsed before the acquisition of data in June 1980, one (Wink 2) collapsed after the images were acquired in May 2002, and a region (Wink 3) is showing developing subsidence within the time period covered by the data.

Due to the fact that Wink 2 collapsed after the images were taken, this data set was considered de facto ground truth and was used for validation purposed in all the algorithms we developed.

Results

We applied the described method to three areas of interest within the previously described dataset: points proximal to Wink 1 and Wink 2, as well as those close to Wink 3. Figure 26 (left) show the segmentation achieved for each subset (black splines) plotted against the point cloud used (color-mapped by displacement). We used cumulative displacement data selected from an arbitrarily late entry in the displacement time series in order to reflect long-term ground behavior. This displacement has a range of -289 mm to 95.5 mm, and a mean of -8.64 mm. For all subsets, the following parameters were employed: $\alpha = 0.1$, $\beta = 1$, $\gamma = 2$, $\lambda = 0.5$, d_{low} = -115 mm, d_{high} = -99 mm.

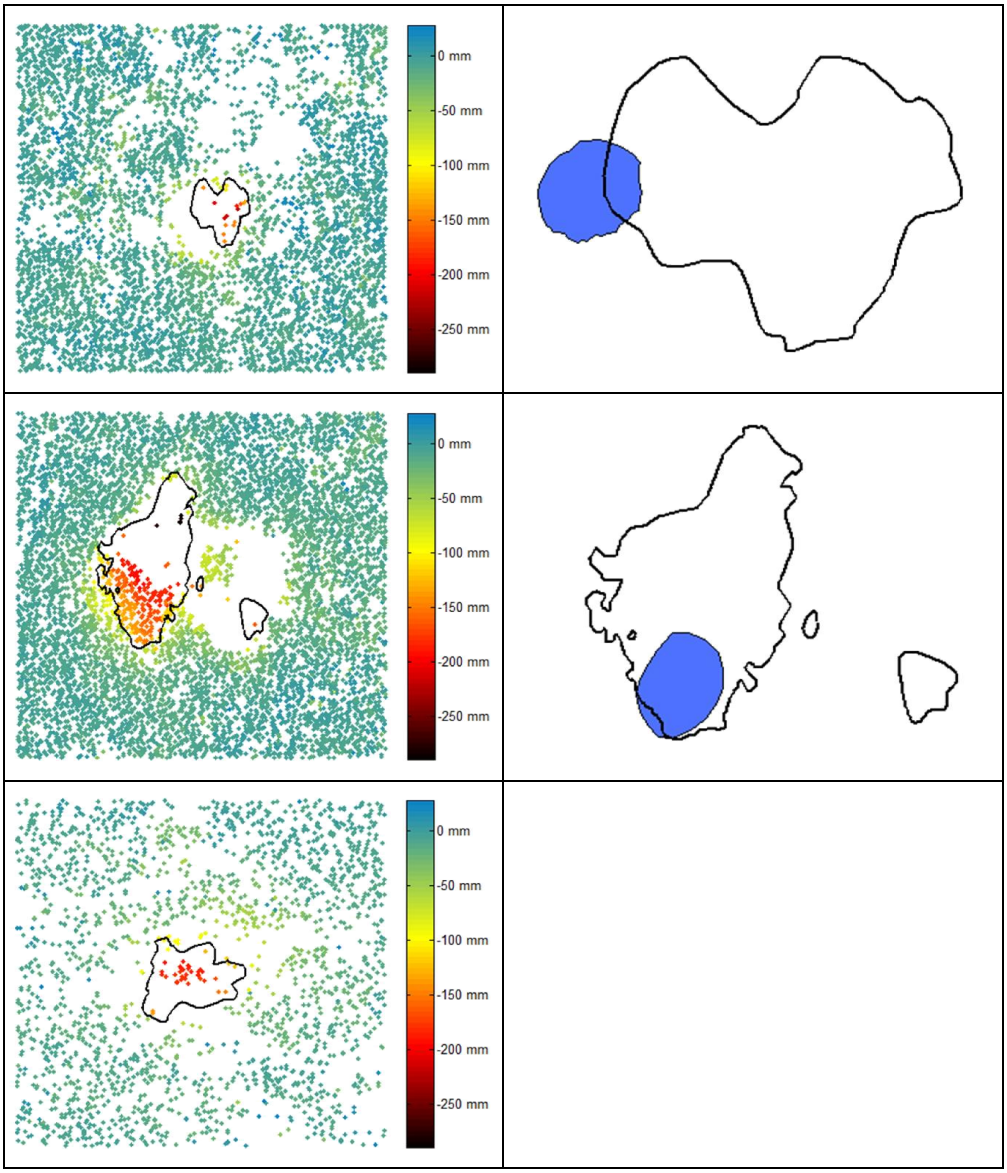

Figure 26 - Results of graph cut algorithm when applied to the sinkhole data set. Detail of the segmentation profile (black line) plotted against the average displacement for the three sinkholes (left). In blue is the actual sinkhole opening plotted for reference together with the profile (right).

In Figure 26 (right) we also show the segmentation of sinkhole forming region for Wink 1 and Wink 2 alongside their respective ground truth. It is important to notice that

the high level of sensitivity offered by the SqueeSAR technique allowed the detection of minute changes influenced by the subsidence in ground displacement over a much larger area than the collapsed section. Nevertheless, as shown in Table 7, we capture about 27% of Wink 1, and 94% of Wink 2. We do not capture a significant portion of Wink 1; however, this sinkhole had already collapsed (and mostly filled with water) before the acquisition period even began, and thus presented poor scattering characteristics for incident radar energy. This resulted in a lack of data over much of the area in and surrounding Wink 1. Wink 2, on the other hand, collapsed after the data collection period ended thus, we had sufficient point density to provide a more robust detection.

Table 7 - Sinkhole detection vs. ground truth.

	Total Area of Sinkhole	Area Within Segmentation	% Detected
Wink 1	8,476 m^2	2,306 m^2	27.20%
Wink 2	5,098 m^2	4,775 m^2	93.67%

Parametric spatiotemporal approach

The graph cut algorithm provides flexibility in the definition of energy function and it was successful in identify the location of the Wink sinkholes that collapsed as well as the still growing depressions. We also successfully applied this algorithm to the Virginia data (that we will describe in the next section). During this process we realized that although efficient, the graph cut algorithm was not landing itself to directly incorporate one of the main features provided by the SqueeSAR algorithm: the time series of displacements available for each point.

Incorporating the time information included in the data within a detection environment required the development of a new approach where spatial and temporal information were considered simultaneously. To achieve this result, we coupled concept from matched filter [12] with the parameter space search at the basis of the Hough transform [13].

The fundamental steps of this approach can be identified as:

1. Define a spatiotemporal model describing the expected changes in crustal elevation due to the feature of interest. What we are interested in describing are the changes to the local elevation rather than the actual shape of the feature of interest. This is required by the differential nature of the DInSAR measurements at the basis of SqueeSAR.
2. Identify the parameters regulating the model behavior. For example, in the case of a sinkhole, the parameters will identify the displacement characteristics: size, orientation, growth velocity, etc.
3. Quantize and define limits of the parameter space.
4. For each point in the parameter space generate the corresponding template (model).
5. Search the data for regions whose spatiotemporal behavior matches the current template.

Feature modeling

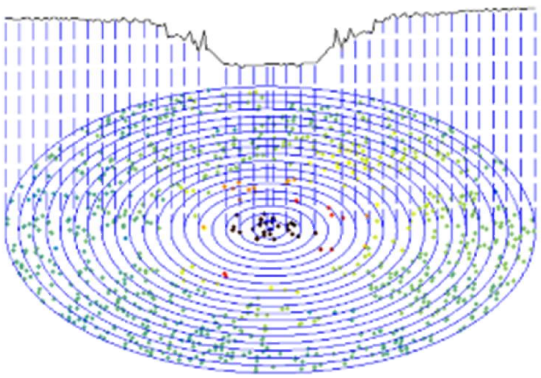

Figure 27 - Construction of displacement profile.

The described algorithm requires the definition of a spatiotemporal model. We focused on the detection of subsidence due to potential sinkholes because, contrary to landslides and bridge settlement, which typically have known locations, sinkholes present the extra challenge of localization.

To define the model, we started by analyzing the spatial changes in the profile of the known sinkholes from the data set described above. Figure 27 provides an illustration of how the profiles where evaluated. Concentric region 5m apart were used to evaluate the average displacement at a given distance from the center of the developing sinkhole. All the points contained in the annuli were averaged and plotted vs. the distance from the center. This process was repeated for all the time frames available and for Wink 2 and Wink 3. The profiles were then plotted next to each other to provide a spatiotemporal graph illustrating the evolution of the profiles (Figure 28).

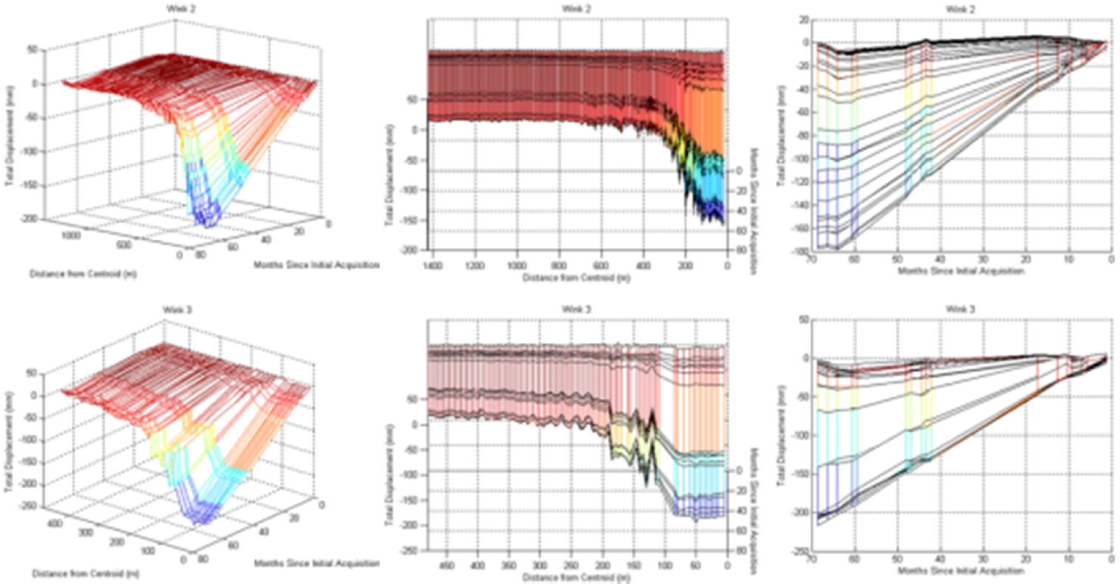

Figure 28 - Spatiotemporal evolution of Wink 2 and Wink 3 profiles. The second and third columns provide projections of the graph on the spatial and temporal plane respectively.

By observing the spatial profiles we evaluated the spatial shape of the deformation to resemble a Guassian of fixed width (identified by σ) while, in the temporal dimension, we observed the linear behavior of the average of the displacements within each of the annuli. We formalized these findings by defining the spatiotemporal model of a growing subsidence as:

$$g(\boldsymbol{x}, t) = \alpha t \exp[-(\boldsymbol{x} - \boldsymbol{x_0})^2 / 2\sigma^2] \qquad (11)$$

This model was verified by evaluating the normalized cross correlation between (11) and each profile obtained from the process described above. After a settling period where the deformation was too small to be identifiable the correlation coefficients reached the asymptotic value larger than 0.97 indicating almost perfect correlation.

Method

Equation (11) represents the basic template used when searching the pointcloud data set. This model is regulated by a parameter vector $\boldsymbol{p} = [\alpha, \sigma, x_0, y_0]$ where α represents the rate of growth of the displacement, σ represents the width of the displacement and (x_0, y_0) is the geographical center of the developing subsidence.

As previously described, once the parameter regulating the model are identified, a parameter space is generate and quantized and, for each point in the parameter space, a well-defined spatiotemporal template $g_{\boldsymbol{p}}(\boldsymbol{x}, t)$ is constructed and a *region of influence (ROI)* identified. In our case, due to the nature of the template, we defined the ROI to be a circular area of radius 3σ centered in (x_0, y_0). The ROI is used to select the data points (from the SqueeSAR pointcloud) that will be considered for matching purposes.

Since what we are interested in is the detection regions displaying a specific spatiotemporal behavior, we defined a scale invariant measure to evaluate the proportionality of the match rather than the actual absolute residual as is typical of ℓ^p norms:

$$\mu(\boldsymbol{x_i}, t) = \min\left(\frac{res(\boldsymbol{x_i}, t)}{\max\left(|d(\boldsymbol{x_i}, t)|, \left|g_{\boldsymbol{p}}(\boldsymbol{x_i}, t)\right|\right)}, 1\right) \tag{12}$$

where the pointcloud data set is represented as $d(\boldsymbol{x_i}, t)$, $\boldsymbol{x_i}$ are the coordinates of the scatterers (PS or DS) and t is the discrete series of relative SAR acquisition times with $t = 0$ representing the first image (for which $d(\boldsymbol{x_i}, t) = 0\ \forall \boldsymbol{x_i}$) and $res(\boldsymbol{x_i}, t) = \left|d(\boldsymbol{x_i}, t) - g_{\boldsymbol{p}}(\boldsymbol{x_i}, t)\right|$.

The overall residual for a given parameter vector $\boldsymbol{p}$ is obtained by averaging the values of (12) calculated for each point in the ROI for each time slice available in the data resulting in a residual matrix $r(\boldsymbol{p})$ of the same dimensionality as $\boldsymbol{p}$.

Results

For validation purposes, we applied this algorithm to the Wink sinkholes dataset which resulted in the correct identification of the regions of active subsidence (Figure 29).

We then applied this approach to the data obtained over the AOI defined as part of this project and obtained a residual map $r(\boldsymbol{p})$. The range of parameters was selected to provide coverage of the entire area $0\text{m} \leq x_0 \leq 43{,}235\text{m}$ $(\Delta x_0 = 2.5\text{m})$, $0\text{m} \leq y_0 \leq 51{,}768\text{m}$ $(\Delta y_0 = 2.5\text{m})$, and allow detection of significant surface deformations $-5\,\text{mm/month} \leq \alpha \leq -1\,\text{mm/month}$ $(\Delta\alpha = 0.25\,\text{mm/month})$, and $5\text{m} \leq \sigma \leq 100\text{m}$ $(\Delta\sigma = 5\text{m})$.

To identify a subset of critical locations for ground verification, we developed a very simple risk function based on the residual function and the amplitude in the template model:

$$\rho(\boldsymbol{p}) = [1 - r(\boldsymbol{p})] \exp\left(1/\alpha_{\boldsymbol{p}}\right) \tag{13}$$

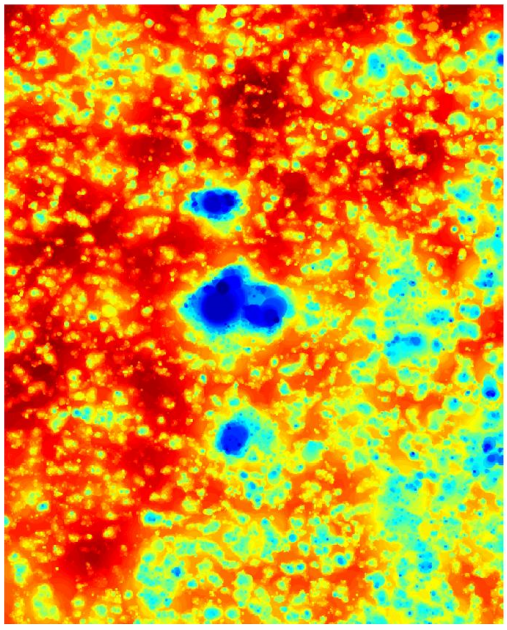

Figure 29 - Spatiotemporal matching applied to the Wink sinkholes data set.

where $\alpha_{\boldsymbol{p}}$ is the α corresponding to the specific parameter space point $\boldsymbol{p}$ considered.

The rationale behind the form of (13) is to provide an increased risk factor for those regions matching faster-growing templates (larger $|\alpha|$ in (11)) while reducing possible false detections by minimizing the risk factor in case of regions showing a slow subsidence grow rate. The risk map was then collapsed according to $m_{\boldsymbol{p}}(x_0, y_0) = \max_{\alpha,\sigma}[\rho(\boldsymbol{p})]$.

Figure 30 shows a comparison between the original average displacement rate (in mm/year) for each permanent and distributed scatterer over the AOI and the risk map $\rho(\boldsymbol{p})$.

Although, as expected, it is possible to identify a general correspondence between subsiding regions and areas of higher risk, the direct comparison highlights the ability of the proposed methodology to distinguish between simple subsidence and subsidence following a modeled behavior.

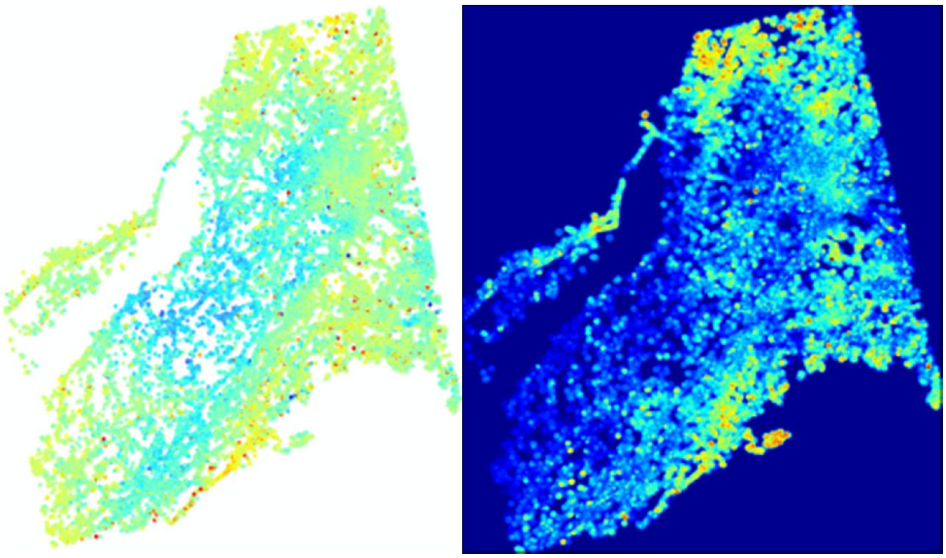

Figure 30 - Average displacement rate of PS and DS (left). Maximum risk m_p obtained from the developed feature tracking algorithm (right).

We classified the regions within the map in four separated categories according to the risk factor: *severe* ($m_p \geq 0.475$), *moderate* ($0.4 \leq m_p < 0.475$), *slight* ($0.35 \leq m_p < 0.4$), and *no risk* ($m_p < 0.35$). These ranges were selected based on the observed behavior of the risk function on the Wink sinkholes data set.

Ground validation

Following this classification, we produced a list of potential subsidence candidates out of which we selected a sample of 32 locations for ground validation: 7 identified as severe, 15 moderate and 10 slight.

Table 8 - Categories of subsidence evidence based on ground inspection.

Categories	Infrastructure	Geomorphology
Absolute (A)	Cracks, settlement	Recent non-vegetated scarps
Strong (S)	Distortions or cracks	Overgrown scarps
Weak (W)	Repairs or cracks	Geomorphology indicates activity
Possible (P)	Near existing active region	In correct terrain, presence of pinnacles
None (N)	No or negative confirmation	No or negative confirmation

To allow for a more direct comparison between the algorithm detection and the ground validation results, we classified the evidence of subsidence in 5 distinct categories based on the observed infrastructure deformation and geomorphology at the inspected location. The categories are listed in Table 8.

Table 9 - Results of ground validation on Virginia AOI.

Risk	Evaluated	A	S	W	P	N
Severe	7	4 (57%)	2 (29%)	-	-	1 (14%)
Moderate	15	8 (54%)	2 (13%)	2 (13%)	1 (7%)	2 (13%)
Slight	10	5 (50%)	4 (40%)	-	1 (10%)	-
Total	*32*	*17 (53%)*	*8 (25%)*	*2 (6%)*	*2 (6%)*	*3 (10%)*

Table 9 shows a direct comparison between the algorithm classification and the ground validation. These results show that 78% of the locations selected between those identified by our algorithm present strong evidence of subsidence.

Software

As part of the project we developed a series of tools that were used to produce the results illustrated in this report. A subset of these tools was packaged as MATLAB scripts and is now available for download from the project website under GPL or BSD licensing. The rest of the tools are currently being translated into the Python language and will be released as Python packages (via the project website and under GPL or BSD licensing) once the translation process is complete.

The following sections provide a brief description of each of the developed tools and how they can be used. A working version of each of these algorithms is included in the DVD delivered as part of this report.

DEM construction software

The digital elevation model (DEM) reconstruction tool was developed in the initial phases of the project and was intended to provide a surface reconstruction approach to be used with the sparse point cloud dataset delivered by TRE. The initial design of our detection approach was centered on the reconstruction of a smooth image to be analyzed using standard image processing techniques. After testing this approach, we observed that the reconstruction process diminished the sensitivity to smaller developing structures. Because of this, the reconstruction was replaced by the direct detection approaches described in this report. Nevertheless, the algorithm was developed as MATLAB script and is available for download from the project website (directory: *Surface Reconstruction*).

Sinkhole detection software

We developed two main detection algorithms, one based on a graph theoretical approach (graph cut) and the other based on a parametric spatiotemporal approach.

Graph cut

The graph cut approach, illustrated in this report (see "Graph theoretic approach" – pg. 41), was developed to provide detection of subsidence, in particular sinkholes, and is tailored to the detection of regions that underwent events and to obtain their separation from the rest of the background.

As our understanding of subsidence features developed, we realized that, although functional, the graph-theoretical approach did not take advantage of the temporal information and, as described in this report, was replaced by the more sophisticated spatiotemporal approach.

Although we are not going to pursue further development of this graph-cut approach as detection mechanism, the algorithm was developed as MATLAB script and will be included in the software DVD, together with a test dataset required to run it, as part of the deliverables (directory: *Graph Theoretic)*.

Parametric spatiotemporal approach

This approach was developed to provide a model independent detection and tracking of features. The main application, illustrated in this report, was targeted towards the detection and parameter extraction of subsiding regions, in particular sinkholes (see "Parametric spatiotemporal approach" – pg.45, for a full description of the functionality of this algorithm).

This algorithm is currently being repackaged as Python package and will be made available for download from the project website under GPL or BSD licensing, once the repackaging is completed.

All current MATLAB implementation of the software and all the data relative to this specific application is included in the software DVD delivered with this report (directory: *Feature Detection and Tracking)*.

Feature tracking software (for bridges and landslides)

Although, as described in this report, the TRE datasets provided indication of slope movements, that were independently verified using photogrammetry and LIDAR (see "Rock slope monitoring" – pg.55), and bridge settlements, that led to the detection of occurring delamination (see "Bridge monitoring" – pg.62), we did not developed a specific model describing these events. Nevertheless, the spatiotemporal matching approach was developed to provide a high degree of flexibility and, thanks to its model independent design, can be used with any template that can be parameterized. In this sense, we believe that it could be successfully used in conjunction with the landslide and bridge settlement models that we are planning to develop as part of future research.

Prototype decision support system

The application of the spatiotemporal matching algorithm to a specific area, results in the generation of a residual matrix (see "Parametric spatiotemporal approach" – pg.45). To provide an example on how this matrix can be used to develop secondary DSS analysis, we have shown how simple risk functions can be developed.

The particular example we provided (13) was designed to increase the relevance of faster growing subsidence events. It is easy to see how the availability of all the template parameters for each detection, can be used to define more complex risk function tailored to specific interests.

The function we defined (13) is currently the main output of the MATLAB implementation of the spatiotemporal approach (see "Sinkhole detection software"). This algorithm is currently being translated into a Python package and will be made available for download from the project website under GPL or BSD licensing, once the repackaging is completed.

Part of the package, the routines necessary to export the results of the analysis to ArcGIS (as shape file) and to Google Earth (as kml files), is already been posted as MATLAB scripts and is available for download from the project website under GPL or BSD licensing (directory: *GIS Export*).

Both MATLAB scripts are included in the DVD delivered with this report.

Conclusions

In recent years new InSAR products providing high resolution temporal information about ground displacement became available. One of the drawbacks of these products is the inherent sparsity of the data resulting from the scatterer selection process required to remove phase errors introduced by the atmosphere and achieve the high measurement accuracy. To overcome this limitation, we introduced a general approach for the detection of spatiotemporal features in point cloud data sets, with particular focus on data sets containing permanent and distributed scatterers.

The presented model-based approach provides flexibility to look within the data for a specific temporal behavior in conjunction with a desired spatial configuration. The results on the Wink sinkhole data set, together with the ground validation performed on the Virginia AOI data set, show that we can successfully isolate regions showing a specific type of subsidence behavior. Nevertheless we would like to point out that, in the case of the ground validation, although signs of subsidence were definite, it was difficult to assess the actual cause of the phenomenon with our preliminary observations. This was mainly due to the high sensitivity provided by the measurements: the largest observed displacements over the measurement period were of the of the order of 30-40mm. So although the behavior of such regions showed a coherent movement in line with our model, it will require a longer observation campaign to precisely determine the cause of the observed subsidence.

We believe that this feature tracking approach, thanks to its model-based design, can easily be integrated into the automated routine monitoring of risk areas and several selected feature types to provide early warnings of the development of hazardous conditions.

Field validation studies

Before the InSAR acquisition started, VDOT personnel selected 7 locations with the area of interest, corresponding to rock slopes adjacent to highways (Table 10). These locations were to be scanned by ground-based LiDAR and Digital Photogrammetry (DP) equipment to determine change in surface profile due to rockfall. The objective was to compare the results with those provided by InSAR. The LiDAR analysis was performed by VDOT personnel; the DP analysis was conducted by Professor William Niemann of Marshall University.

Table 10 - Ground validation locations (Figure 31).

Code	Location
RS-629-001	Route 629 (Deerfield Road)
RS-629-002	Route 629 (Deerfield Road)
RS-629-003	Route 629 (Deerfield Road)
RS-064-001	Interstate 64, southeast of Staunton
RS-600-001	Route 600
RS-042-001	Route 42
Greenville Riprap Slope	Rock buttress at Greenville School Road

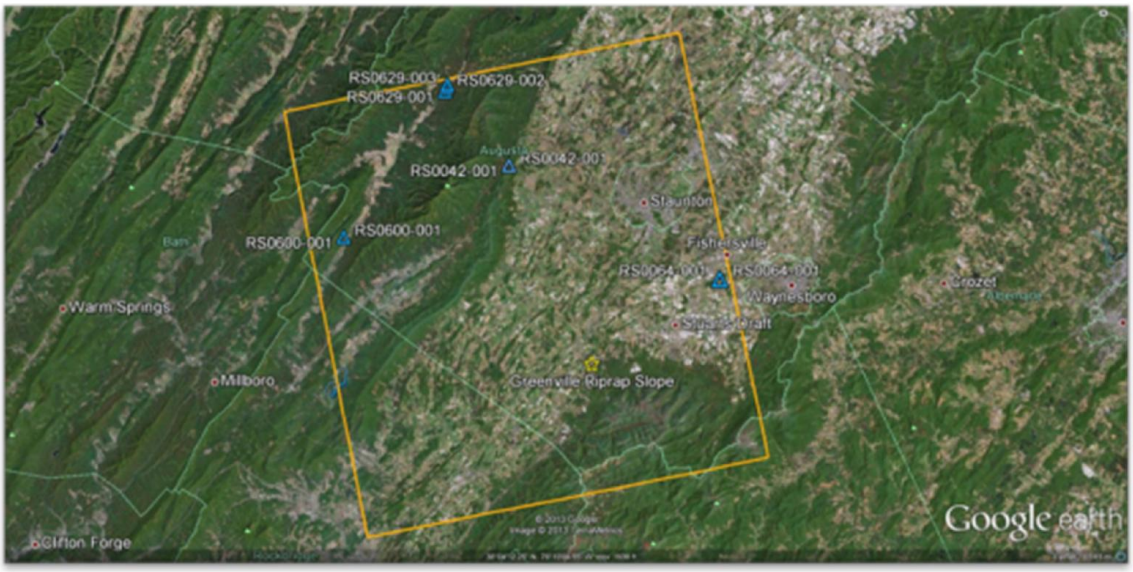

Figure 31 - Slope locations for field validation studies.

Photogrammetry is the practice of determining the geometric properties of objects from photographic images. Photographs for this purpose can be taken from different perspectives; a general distinction is often made between aerial and ground-based photogrammetry. The field photographs for this project were taken with a tripod-mounted Nikon D-90 digital camera and a 24-millimeter lens. At each site, photographs were taken at each of two camera positions according to the geometry shown in Figure 33 in order to create photo pairs. In addition, a spray-painted reference point, or Ground

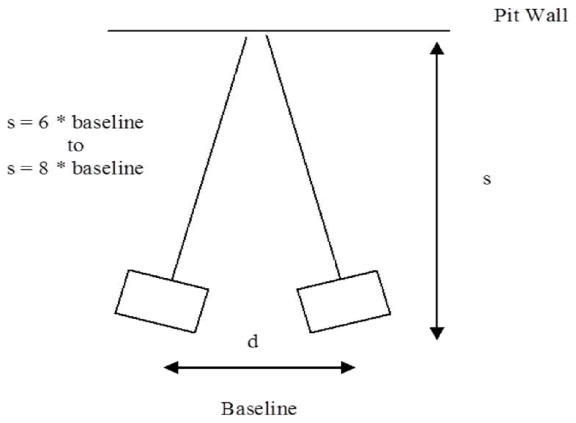

Figure 33 - Generic layout of camera position (rectangle) and subject slope for DPG. Spacing between camera position (d) should be 6-8 times the distance (s) from baseline to subject slope [6].

Control Point, was established on the rock face. Data processing was carried out using Sirovision software. Sirovision is a mapping and analysis system that can generate 3D images of rock faces from stereo photographs. The software was originally developed for mining applications.

LiDAR technique involves High Definition Terrestial Scanner (HDTS) projecting laser light on the area of interest and recording the reflections. The system creates a point cloud of light pulses. The time of flight from the scanner to the target and back to the scanner is recorded individually for each laser pulse. In addition, each point is georeferenced to allow GIS processing. The results are high resolution 3D surface images of the scene. Change detection can be quantified by comparing digital images obtained from scans collected on different dates. LiDAR technique can capture topographic information and provide inventory of surface characterization. Projects such as scanning busy intersections, bridges, or complex surfaces can be scanned quickly and accurately.

Figure 32 - Leica HDTS system.

Tripod-mounted Leica HDS3000 long range scanner, as shown in Figure 32, was used in this study. This scanner has 360 degrees horizontal field of view and 270 degrees vertical. All point cloud data at each site were collected from a single setup. LiDAR surveys for this study were performed by VDOT personnel. Data processing of the point cloud was carried out with the help of the TopoDOT software.

LiDAR and DP scans were started before InSAR results were delivered, to establish the baseline readings. Due to the subsequent InSAR data frame alignment, four out of the seven locations resulted in being just outside the area scanned by the satellite. The only sites with both satellite and ground-based verification data available were the rock slopes on Route 600, Route 42 and the rock buttress at Greenville School Road. The site at Route 600 was the only one where InSAR, LiDAR, and DP data were collected. No InSAR results were generated at the Route 42 site. Both LiDAR and DP detected very small changes in slope surface profile at that location. The rock buttress at Greenville Road was not accessible for LiDAR scanning, but InSAR and DP techniques detected some movement.

Rock slope monitoring

Rock slope monitoring was carried out at the Route 600 site, located near the western boundary of the AOI. The site, as shown on Figure 34, consists of dipping slopes of dark blue-gray, fine to medium-grained cherty limestone of the Silurian and Devonian age. The slope height and angle are approximately 37 m (120 ft) and 40 degrees, respectively. Chert content causes the slope surface to be rugged. The rock mass is heavily jointed. Material is released where the joints intersect the bedding planes. This slope presents a continuous maintenance problem for VDOT.

Figure 34 shows TS results (color tiles) with some DS points superimposed (cyan circles). TS data are shown using a color scheme, with red intensity proportional to displacement. No PS points were detected at this site. Example time-displacement graph is shown for a DS point (A002Z).

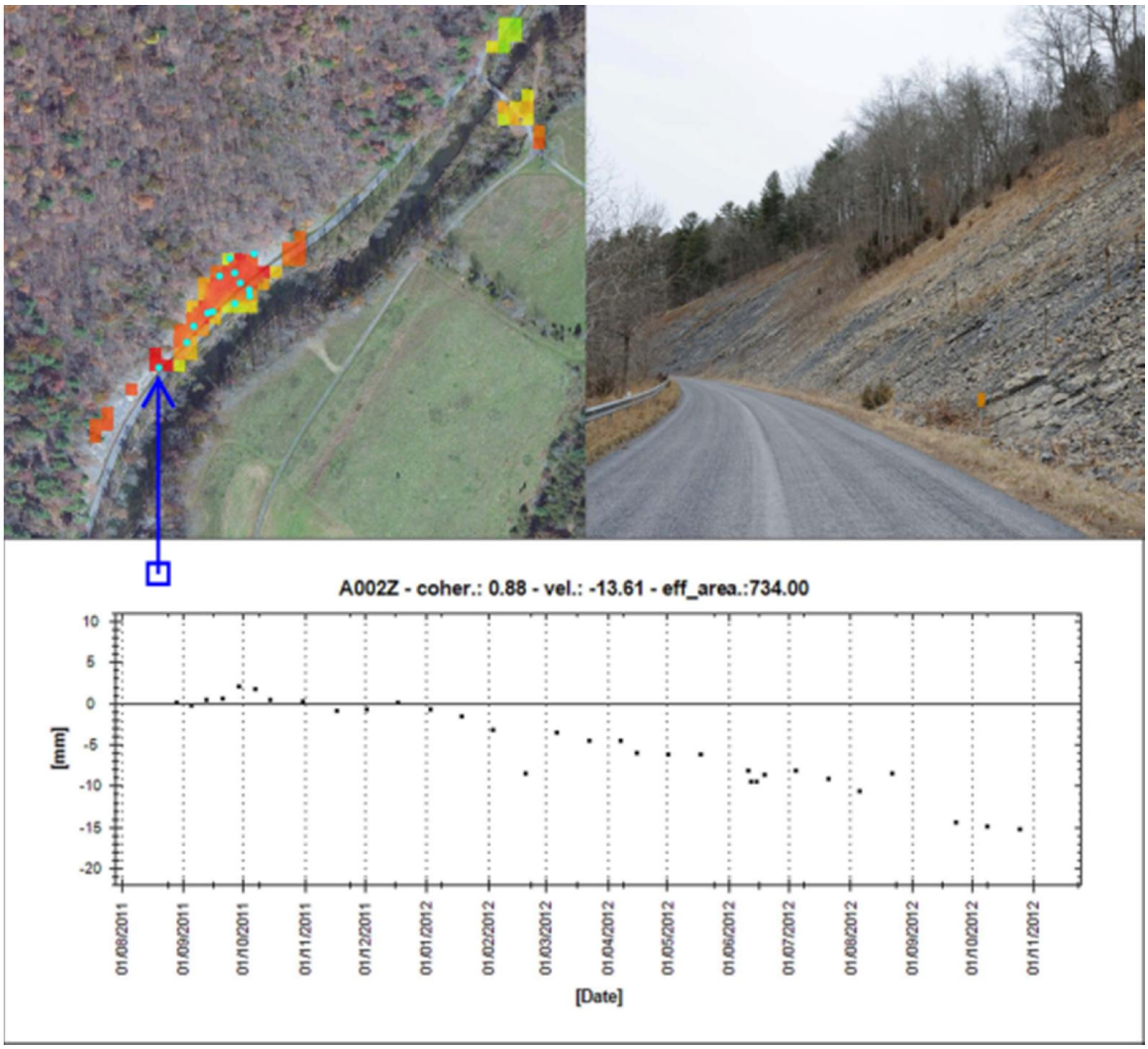

Figure 34 - Route 600 rock slope monitoring using TS and DS data.

In addition to InSAR analysis, this slope was also the subject of ground-based LiDAR and Digital Photogrammetry (DP) field validation studies. The results obtained from

InSAR, LiDAR, and DP data are fairly consistent and indicate approximately 20 mm (0.8 in) change in rock surface elevation during the monitoring period.

Digital photogrammetry and LiDAR are both point-cloud data collection methods, which yield an XYZ file that can be brought into a GIS (or other geospatial) dataframe. This allows three-dimensional analysis of the rock slope. Sirovision software was used to generate scaled 3D images of rock faces from stereo photographs. A second module, Sirojoint, was used for limited geotechnical and structural analysis of the 3D images. The data resulting from Sirovision was then brought into ArcGIS software, and surface analysis was used to interpret the kinematics and geomechanics.

Figure 35 is an aggregate of the digital photogrammetry data and interpretation brought into an ArcMap dataframe, and relates the field conditions to the GIS analysis. The surface analysis highlights portions of the slope of different azimuthal aspect. The yellow wedges are surfaces formed by the intersection of the joints and the bedding. The purple colors represent incoherent slope aspect along the entire toe of the slope, indicating a broad failure mode along its entire length.

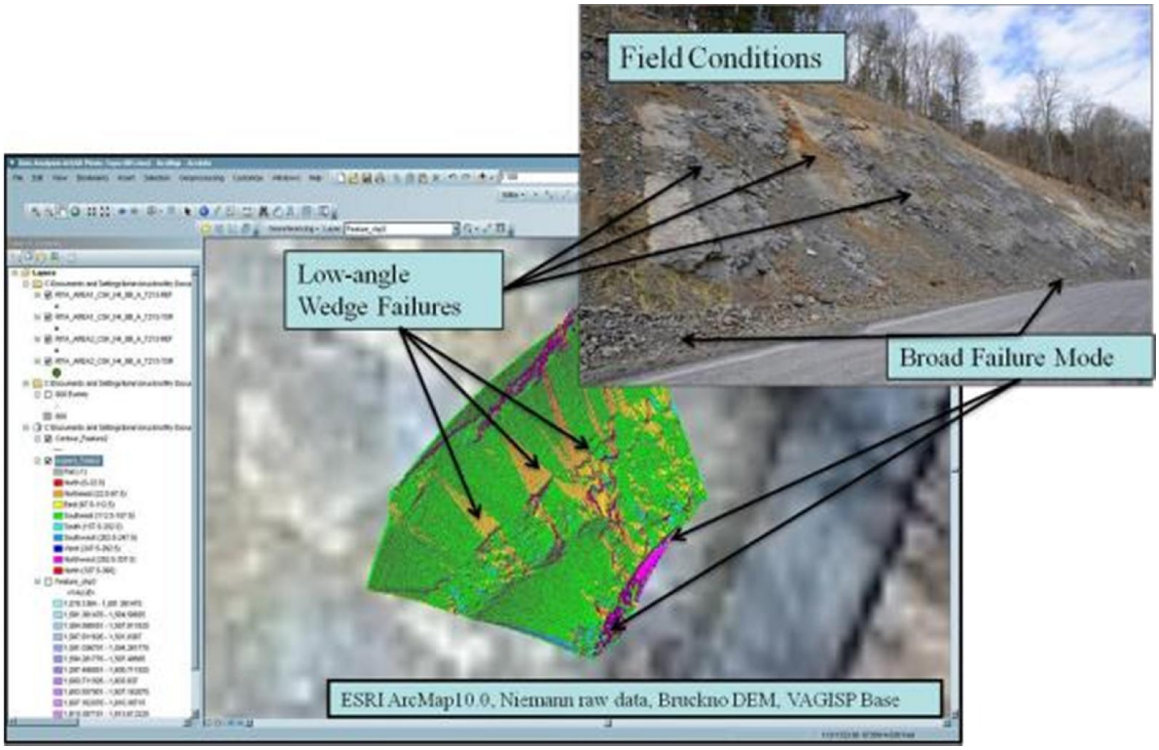

Figure 35 - RS-600-001 Digital Photogrammetry Data.

Figure 36 is an aggregate of the digital photogrammetry data and interpretation brought into an ArcMap dataframe, and the stereonet represents of site kinematics.

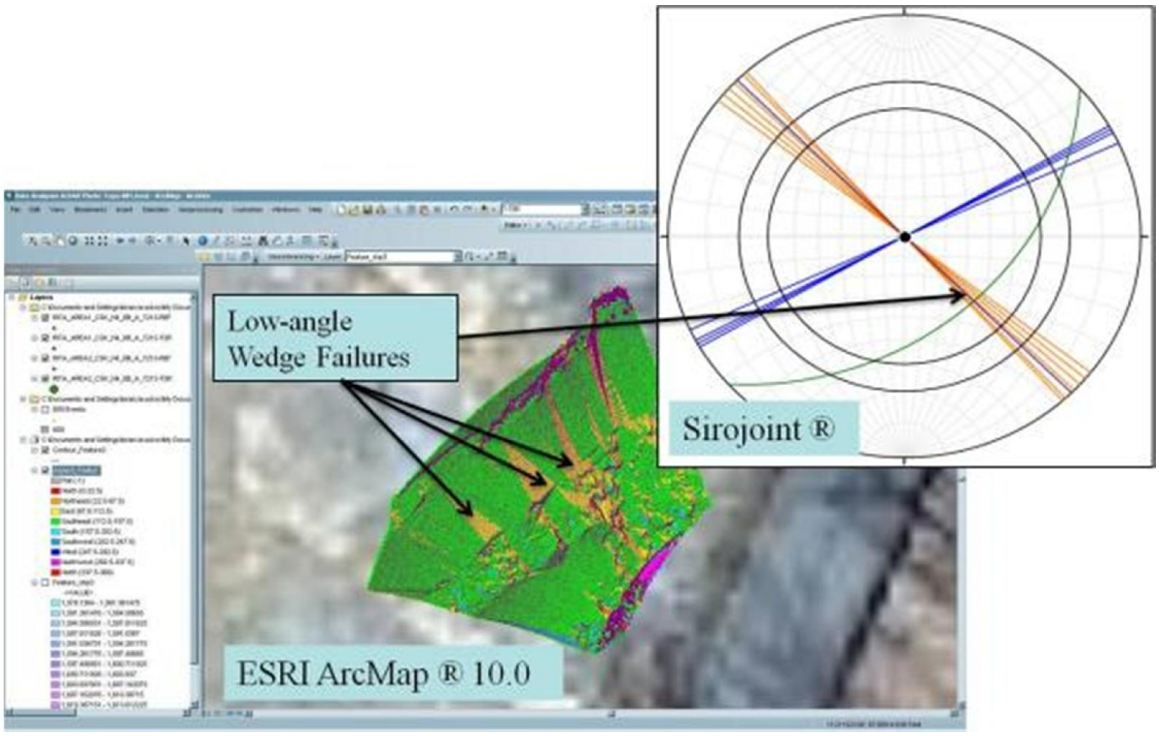

Figure 36 - RS-600-001 Digital Photogrammetry Data and Analysis.

Both the digital photogrammetry and the GIS interpretations agree well with the field conditions: Sirojoint reveals a systematic set of wedge failures formed by the intersection of moderately-dipping bedding and high-angle joints. The GIS surface aspect analysis reveals the wedge failures to be pervasive along the rock slope surface. The data yielded by the LiDAR consist of a set of point cloud data overlapping the digital photogrammetry data and yielded similar results and interpretations. The InSAR data agrees with the field conditions as characterized by GIS and digital photogrammetry.

Greenville School Road riprap slope

The AOI contains a number of riprap-covered slopes. Typically, riprap stone is placed on the slope to stabilize it and prevent failure. In general, riprap surface was found to be an excellent InSAR scatterer.

Figure 37 shows InSAR points at the riprap slope along Greenville School Road. Figure 38 represents time series of displacement of some scatterers on the riprap surface. This site was identified early in the monitoring period as a potential zone of movement, based on preliminary InSAR data. Several site visits, as well as two episodes of digital photogrammetry data collection, were conducted. Figure 39 shows an image of the DP data along with the site photograph.

Figure 37 - InSAR points at the riprap slope along Greenville School Road.

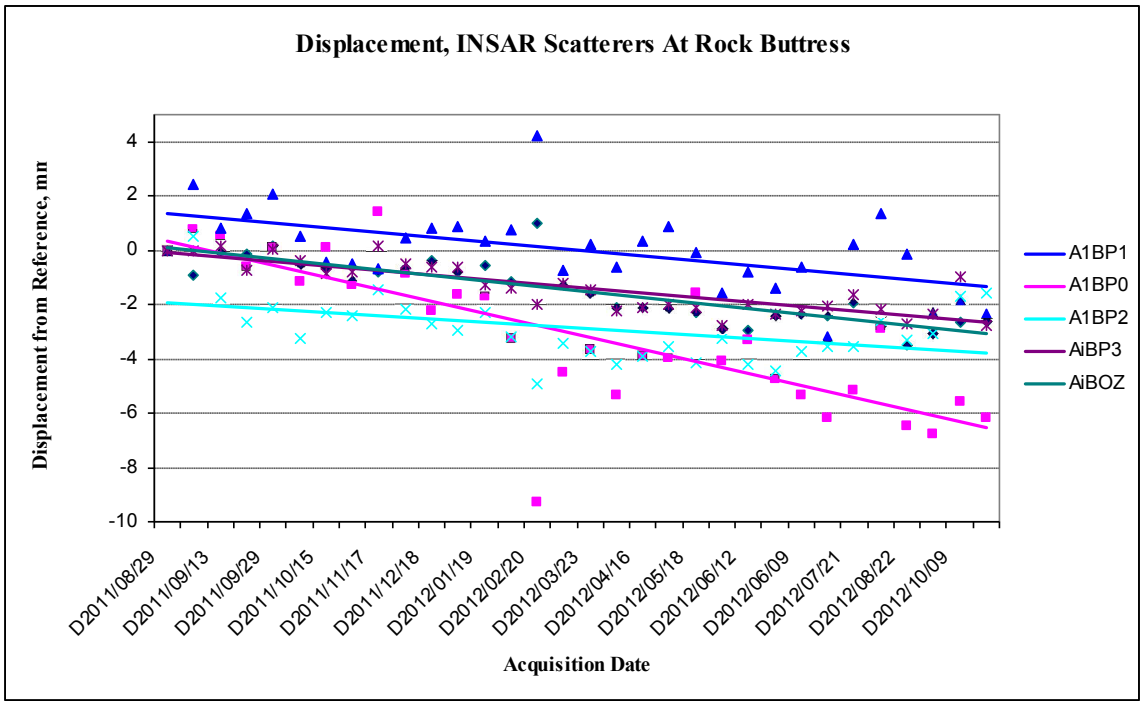

Figure 38 - InSAR Scatterer Data at Rock Buttress.

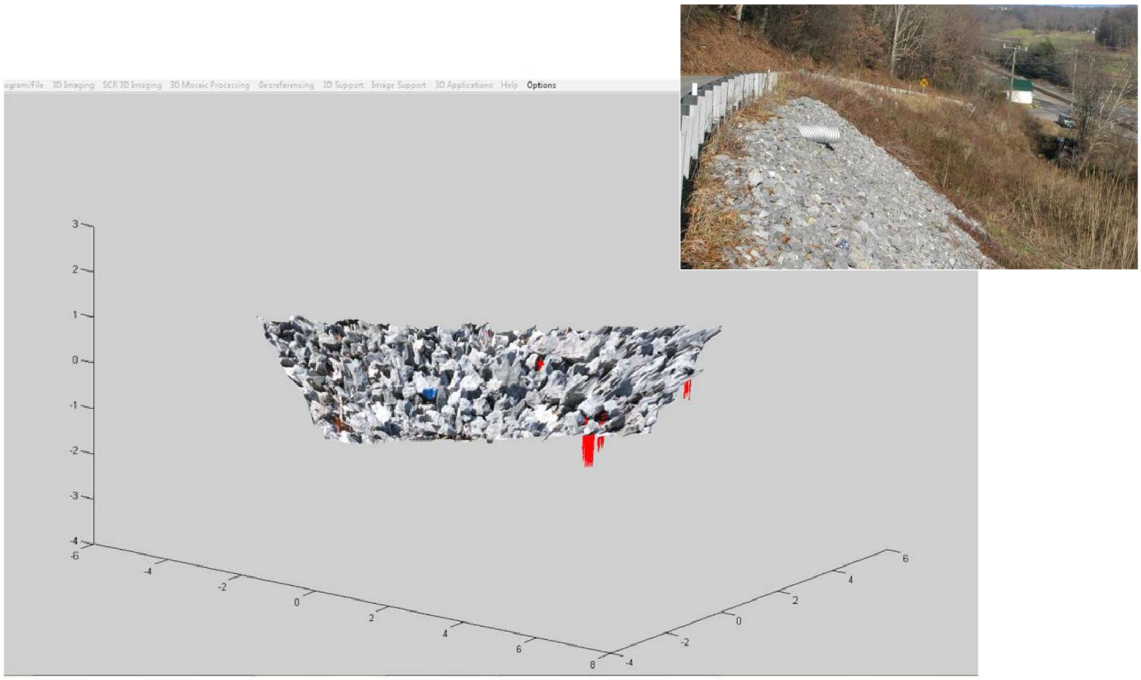

Figure 39 - Sirovision® Photogrammetric Image at Rock Buttress.

The red lines show area of maximum calculated displacement at the rock buttress slope between September and November 2012. Field investigations at the site indicated that a combination of internal settlement and blocked drainage pipe is causing the surface of the rock buttress to distort, and may indicate a risk of future failure. InSAR results revealed previously unidentified slope movement.

Figure 40 - Site Conditions and Deterioration at Rock Buttress.

Sinkholes

The primary focus area of the study was automated detection of subsidence behavior indicative of the onset of sinkhole formation. The majority of karst features encountered in the Valley and Ridge physiographic province are of the solution-type sinkhole. They are characterized by water-soluble bedrock and the overlying soils. As joints and discontinuities within the soluble bedrock material widen, they are filled in by surface soils, resulting in a characteristic depression. In such cases, sinkhole development is a relatively slow and progressive process.

A simplified risk function was developed to identify a risk factor based on the computed rate of growth of local subsidence. Severe, moderate, and slight risk areas with the corresponding location coordinates were identified. Ground validations were carried out, which indicated that 78% of selected locations showed strong evidence of subsidence. Figure 41 shows a sinkhole detected in a residential subdivision near Staunton based on spatiotemporal modeling of InSAR PS and DS data points.

Figure 41 - Sinkhole detected in a subdivision near Staunton.

Another approach to local subsidence detection involved analysis of TS raster data. The underlying assumption is that a point that was coherent at one time may have lost its coherence due to excessive displacement, possibly due to sinkhole development or other ground movement. Figure 42 shows an example of a possible sinkhole development in the City of Staunton. TS data were processed using ArcGIS software. The original grayscale image was converted to a color scheme (red indicates settlement) and the neighboring pixels were averaged.

There is clear evidence of pavement distress at this site. Interviews with city officials indicate that approximately a year ago there was a sewer line break in the vicinity. Local DS point (A4ZY0) shows approximately 15 mm (0.6 in) of settlement during the monitoring period. This part of Staunton has been known for catastrophic sinkhole events in the past. The point of interest is located almost directly over an underground stream (Lewis Creek), which flows parallel to the nearby street in the southerly direction.

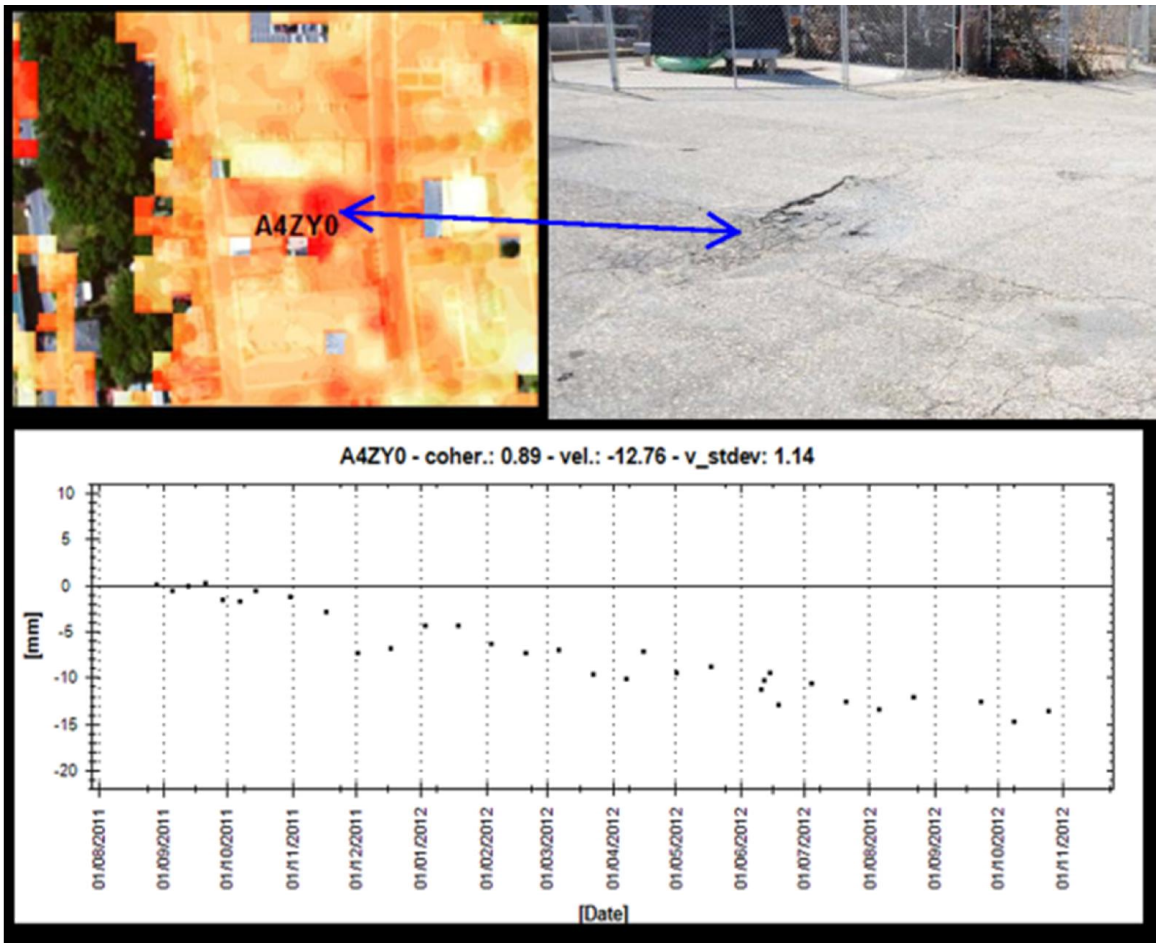

Figure 42 - TS and DS data indicating subsidence in the City of Staunton.

Highway embankment monitoring

TS data were found to be particularly useful for spotting localized differential settlements along roads and adjacent cut or fill slopes. Figure 43 shows an example application near the intersection of Interstate 81 and Route 712. TS data (color tiles) are shown with superimposed DS (cyan circles) and PS points (black crosses).

The construction of a new bridge over I-81 and approach embankment at Route 712 was completed just prior to the monitoring period. TS data indicates substantial post-construction settlements (dark shades of red). Field observations corroborate these findings. Pavement surface at this location exhibits distinct 'wavy' pattern indicating extensive differential settlement.

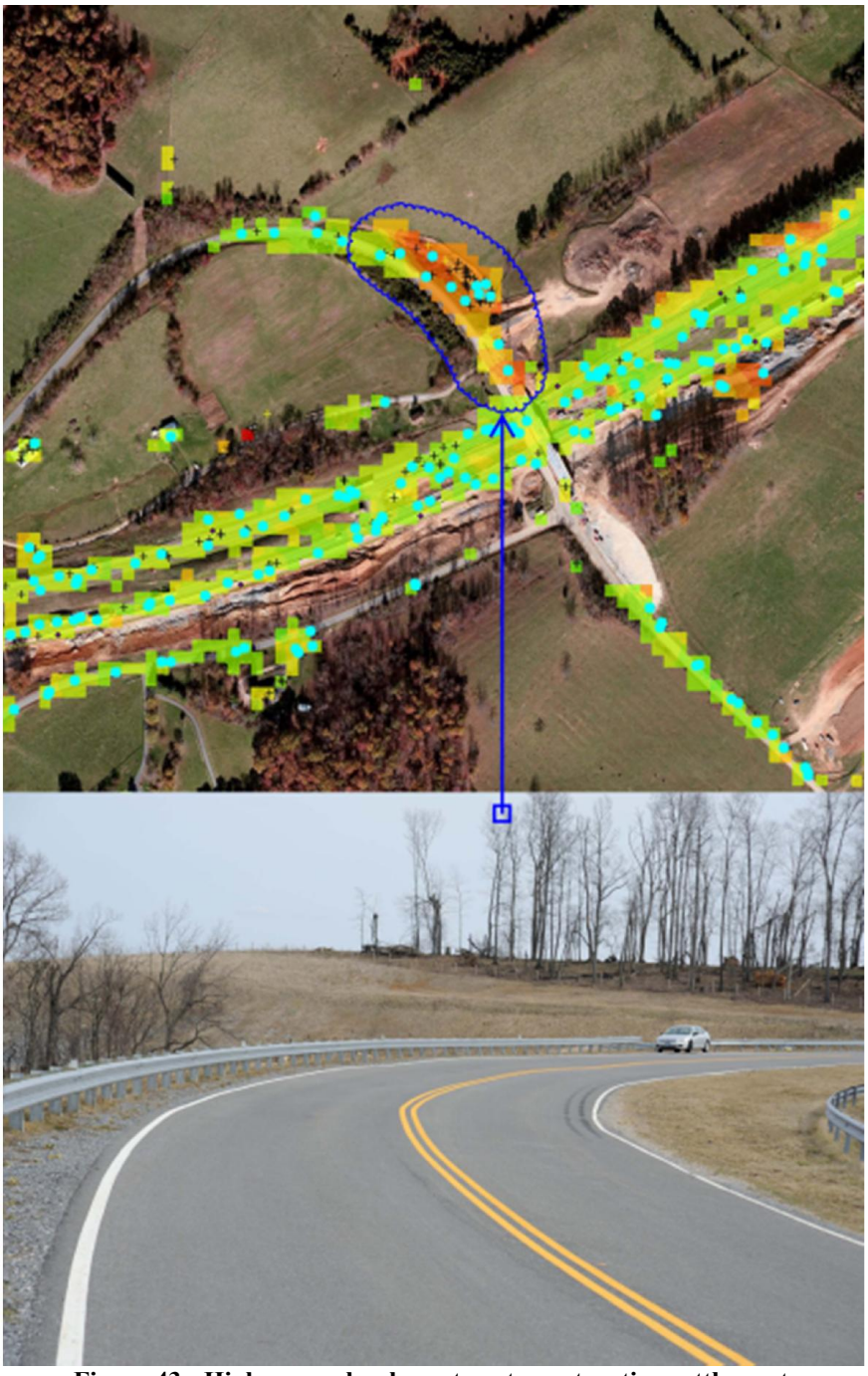

Figure 43 - Highway embankment post-construction settlement.

Bridge monitoring

The use of InSAR for bridge monitoring was found to be challenging. Modern bridges are typically integral or semi-integral constructions, with no expansion joints present on the superstructure. Usually, there are no distinct natural scatterers that can be isolated on the deck surface, except possibly for the steel guardrails attached to the parapets. This makes it difficult to obtain bridge displacement data corresponding to specific points of interest.

Figure 44 shows example InSAR results obtained from an older simple span bridge located at Route 635 over Interstate 81. PS points labeled as PS1 and PS2 align with deck joint locations over bridge piers. The corresponding time-displacement PS data indicate progressive settlement, approaching approximately 5 mm (0.2 in) during the monitoring period. Figure 44 shows the underside of pier cap at location PS1, with exposed reinforcing bars due to delaminated concrete cover. The inspection report documents significant deterioration to concrete and bearings. The bridge is already scheduled for maintenance work. It is possible that there may be some correlation between the InSAR results and the overall bridge condition. The evidence of concrete delamination may be indicative of other deterioration taking place at the pier cap, joint, or bearings, most likely due to chloride intrusion.

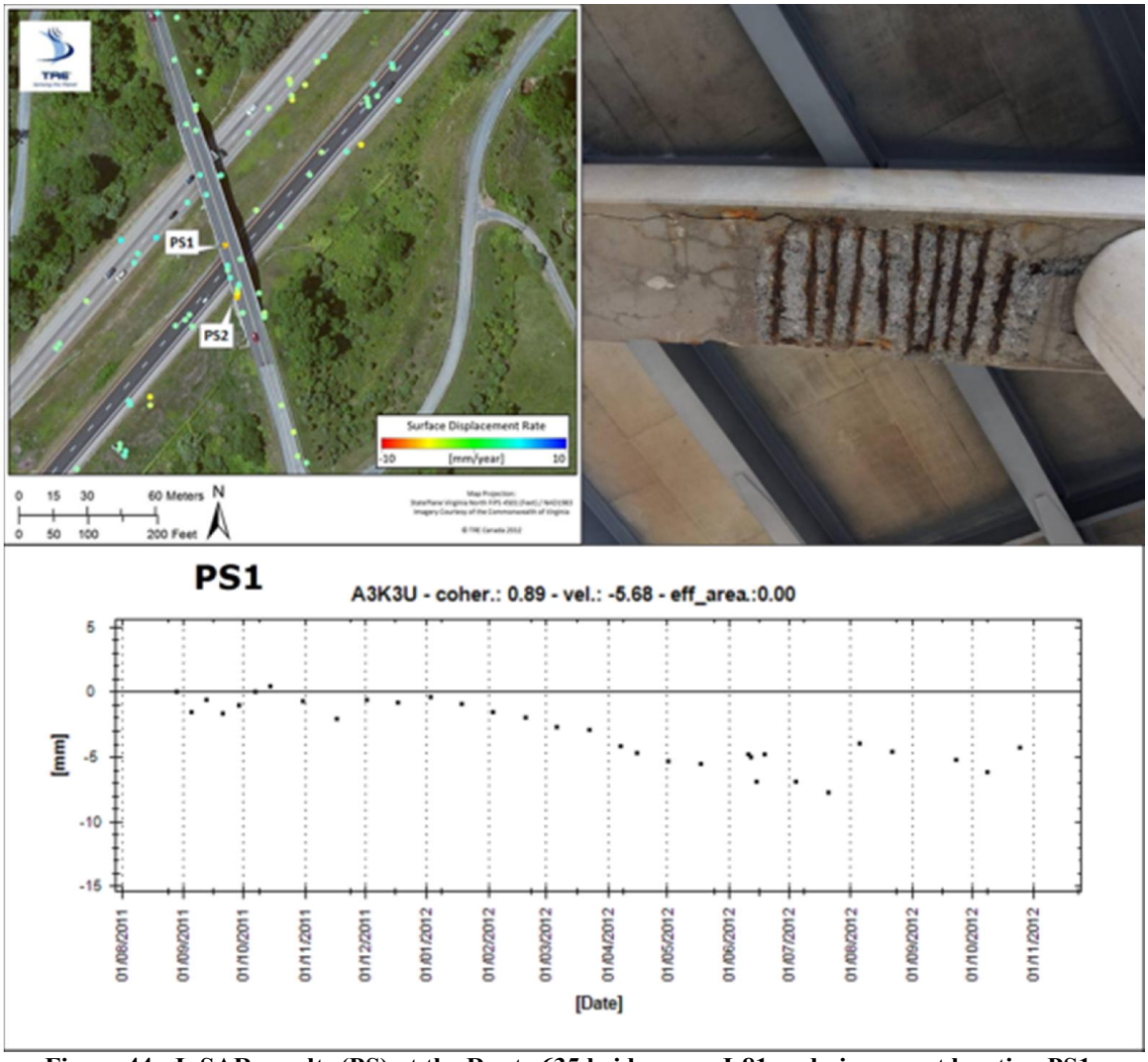

Figure 44 - InSAR results (PS) at the Route 635 bridge over I-81 and pier cap at location PS1..

Figure 45 shows an example of a railway bridge in a fairly poor condition. InSAR data at this location included points indicating relatively large settlements at the superstructure.

Figure 45 - Railway bridge with high InSAR displacements.

Figure 46 shows deteriorated railway ties found at the location corresponding to a high settlement.

Figure 46 - Deteriorated railway ties at the location of high settlement..

To address the problem of obtaining displacement data at specific points on the bridge, the researchers experimented with the use of artificial radar reflectors. Typically, these are dihedral and corner reflectors constructed from steel plates. The required size

makes them impractical to use on a typical bridge superstructure due to safety concerns. Consequently, it was decided to carry out experiments with much more compact, spherical in shape, Luneburg lens reflectors. Their internal design, involving layers of materials with varying electrical permittivity, allows the radar signal to be reflected directly towards the point of origin regardless of the angle of incidence, to provide an effective local scatterer. Typically, Luneburg lens reflectors are used to track moving targets. They have not been used in transportation InSAR applications to date.

Figure 47 shows a load test setup on the Route 262 bridge over Route 250 in Amelia County. The bridge is a 38.4 m (126 ft) long single span semi-integral structure. Three Luneburg lens reflectors with varying radar cross-sections were affixed to the parapet and one to an abutment wingwall to provide a fixed reference.

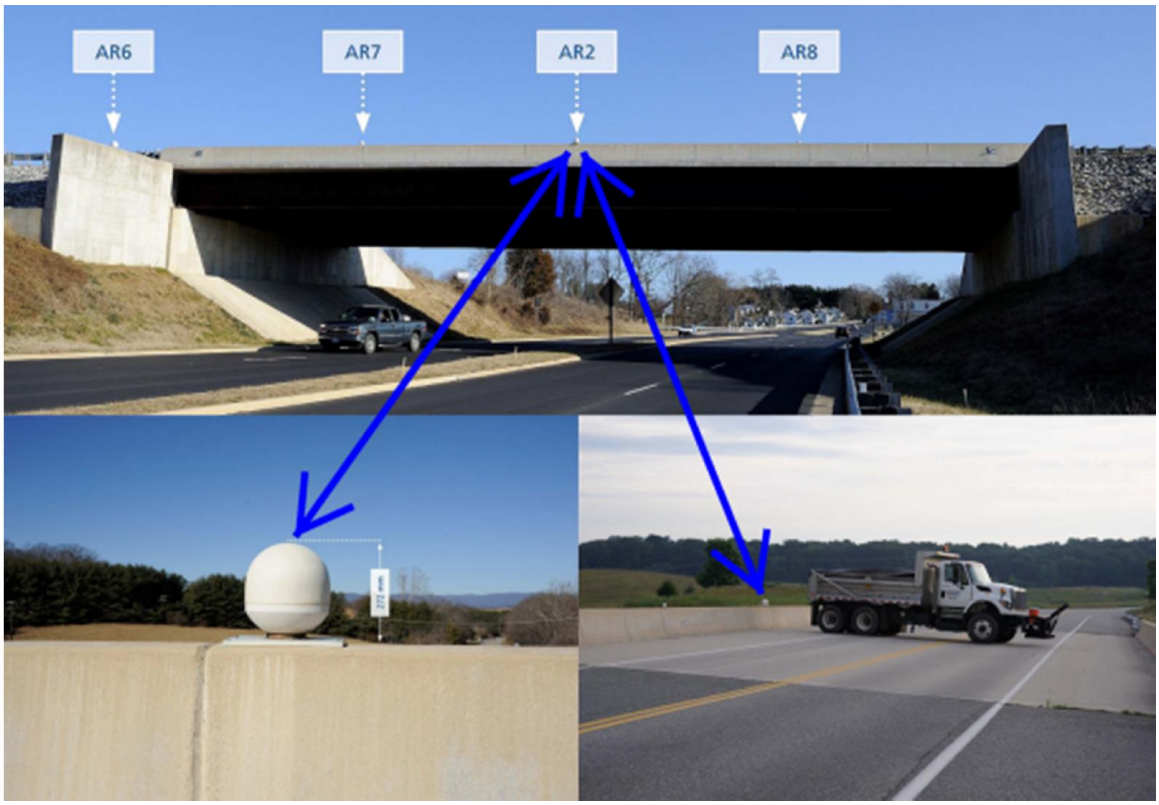

Figure 47 - Load test setup at the Route 262 bridge over Route 250.

The bridge was closed to traffic approximately 15 minutes prior to the scheduled satellite overpass. A heavily loaded dump truck was parked transverse to traffic at mid-span, close to the parapet with Luneburg lens reflectors. The applied load was 24.8 metric tons (54,620 lb). The resulting mid-span deflection at the parapet, as determined by conventional survey technique, was only 3.4 mm (0.13 in). Although the return signals from artificial reflectors were visible in the radar imagery, no measurable InSAR deflections were detected. The results may have been overshadowed by the estimated ±5mm (0.20 in) error range for a single-shot measurement. Part of the challenge involves selection of a suitable radar cross section (RCS) for the Luneburg lens reflector. It appears that a minimum RCS of 10 m^2 (108 ft^2) is required for the X-band radar signal to

register a strong enough reflection. The reflectors used at the bridge had RCS values of 1, 2, 10, and 50 m^2.

Detection of surface erosion

Temporary scatterers (TS) were found to be very useful in identifying areas of localized change, such as surface erosion. Figure 48 shows several isolated TS data points with relatively high magnitude of displacement, as indicated by red squares. They are located adjacent to I-81 North, near Staunton. Subsequent field inspection revealed highly eroded ground surface extending just beyond the guardrail running along I-81. There were no PS or DS points identified in this area. It would have been very unlikely for such erodible surface to stay coherent throughout the entire monitoring period.

Figure 48 - TS points along I-81 (left) and surface erosion at the TS point locations (right).

Pavement monitoring

One of the most promising applications of TS data, discovered in the course of field validation, appears to be pavement condition monitoring. Figure 49 shows examples of TS results from the junction of Route 262 and Middlebrook Avenue, west of Staunton. Significantly different TS responses were recorded on these two roads, correlating to visible evidence of surface distress along Middlebrook Avenue. Similar patterns were observed at other locations.

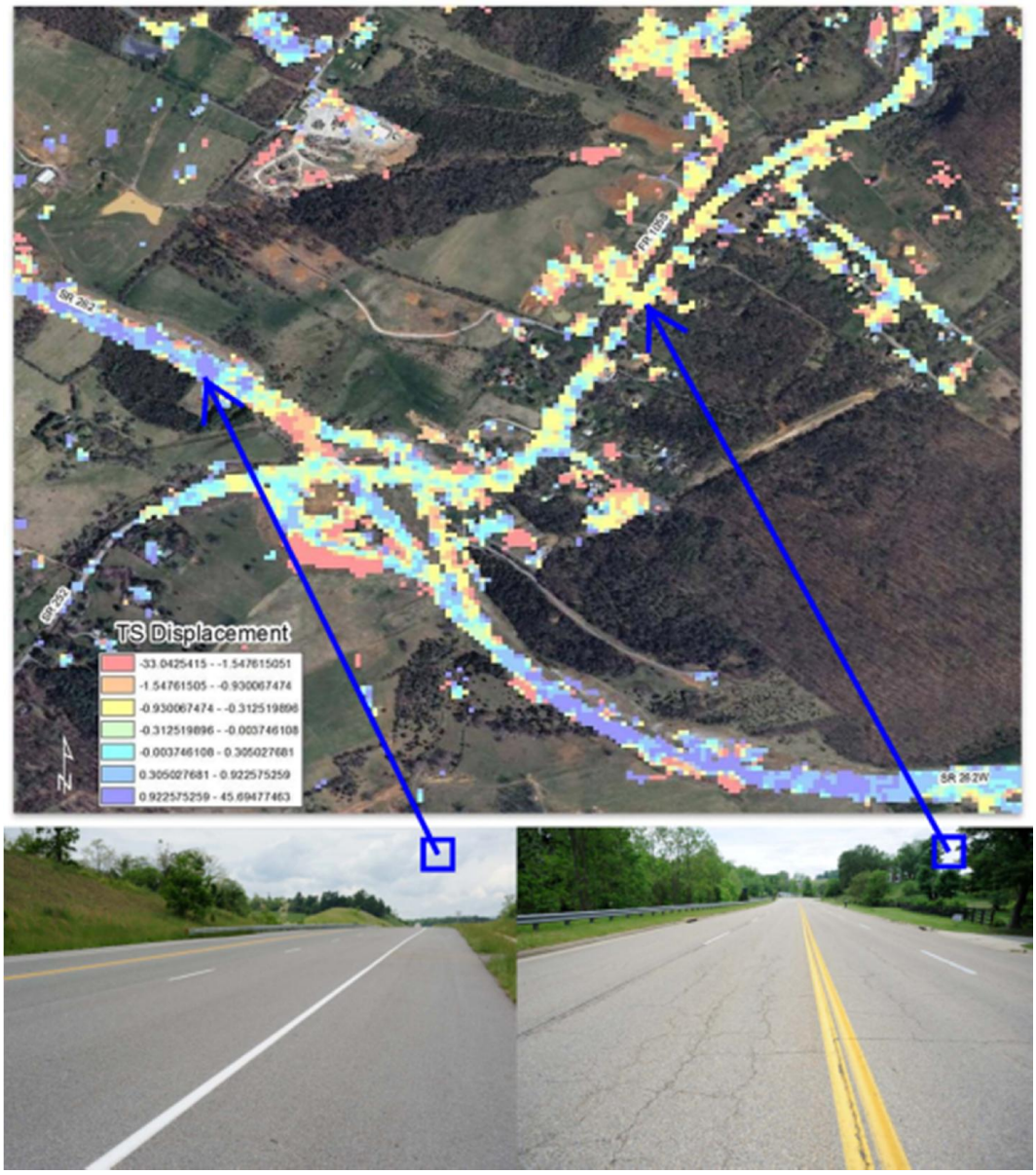

Figure 49 - TS results corresponding to pavement in good condition at Route 262 (bottom left) and one in poor condition at Middlebrook Avenue (bottom right).

Conclusions

In general, the InSAR scatterer data were positively correlated with the field evidence of infrastructure damage or distortion on a range of geotechnical assets including slopes, bridges, and pavements. In most cases there was a direct link between the InSAR data and the observed field conditions. Many InSAR settlement points were correlated with the presence of nearby highway drainage structures. While the AOI allowed analysis of only one rock slope by InSAR and ground-based methods, the results provided by InSAR corresponded to field observations and measurements made by digital photogrammetry and terrestrial LiDAR.

Field validations carried out on potential sinkhole locations indicated high percentage of sites with a localized subsidence. Many of these sites were not actual sinkholes, but their settlement behavior was similar. Examples include a junkyard or a municipal landfill site. Additional refinements to the sinkhole detection algorithm, including masking known areas, can address the problem of false positives.

The results indicate that there are potential practical applications of InSAR to monitoring transportation infrastructure. The scatterer density is generally sufficient for assessing deformation phenomena along the transportation corridor. Sinkhole detection and slope stability monitoring are some of the most obvious geohazard applications to pursue. Others are likely to be developed as the technology becomes more widely implemented. Potential uses include monitoring settlements at bridge approaches, tunnel entrances, drainage structures, retaining walls, and railways.

One of the main attractions of satellite based InSAR is the ability to cover large areas with a predictable and ongoing schedule, making it suitable as a network level monitoring tool. While satellite-based InSAR can be used for supplying pinpoint overview of potential trouble spots, other ground-based remote sensing technologies, such as LiDAR, Digital Photogrammetry or high frequency radar, can be applied for a follow-up detailed assessment of a particular site, as a synergistic approach. The availability of millimeter-scale remote sensing of deformation offers potential new opportunities for effective implementation in transportation, particularly for geohazard assessment.

Publications and Outreach

The results of the research presented in this report were presented at several venues as well as in the form of publications. Furthermore, the interest of the community resulted in secondary reporting in the media.

Publications

Journals

A. Vaccari, M. Stuecheli, B. Bruckno, E. Hoppe, and S. T. Acton, "Detection of geophysical features in InSAR point cloud data sets using spatiotemporal models," *International Journal of Remote Sensing ,* Vol.24, No.22, p.8215-8234, 2013

Conference

E. Hoppe, B. Bruckno, E. Campbell, S. Acton, A. Vaccari, M. Stuechli, A. Bohane, G. Falorni, and J. Morgan, "Transportation infrastructure monitoring using satellite remote sensing," *Proceedings of the Transportation Research Arena 2014*, Paris, France, September 2014

B. Bruckno, E. Hoppe, A. Vaccari, S. Acton, E. Campbell, and W. Niemann, "New Applications for Interferometric Synthetic Aperture Radar [InSAR]: Interpretation of Scatterers for Rock Slope Evaluation," *Virginia Geological Research Symposium*, Charlottesville, Virginia, April 17, 2014

B. Bruckno, E. Hoppe, A. Vaccari, S. Acton, and E. Campbell, "New applications for interferometric synthetic aperture radar [InSAR]: interpretation of persistent, distributed, and temporary scatterers for geohazard and infrastructure monitoring and evaluation," *Geological Society of America Abstracts with Programs*, Vol. 46, No. 3, April 10-11, 2014

B. Bruckno, E. Hoppe, A. Vaccari, S. Acton, and E. Campbell, "New applications for interferometric synthetic aperture radar [InSAR]: Field validation studies of persistent, distributed, and temporary scatterers," *Geological Society of America Abstracts with Programs*, Vol. 46, No. 2, March 23-25, 2014

A. Vaccari, B. Bruckno, E. Hoppe, S. Acton, and E. Campbell, "Delivering geohazard and geotechnical data: From the satellite to the field," *Geological Society of America Abstracts with Programs*, Vol. 46, No. 2, March 23-25, 2014

E. Hoppe, B. Bruckno, E. Campbell, S. Acton, A. Vaccari, M. Stuechli, A. Bohane, G. Falorni, and J. Morgan, "Interferometric synthetic aperture radar applications at the Virginia Department of Transportation," *Transportation Research Board 93rd Annual Meeting Final Program*, p. 35, Washington, D.C., January 12- 16, 2014

B. Bruckno, E. Hoppe, A. Vaccari, and E. Campbell, "Validation of new applications for interferometric synthetic aperture radar [InSAR] data: Geohazards and infrastructure distress," *Geological Society of America Abstracts with Programs*, Vol. 45, No. 7, p.719, October 27-30, 2013

A. Vaccari, and S. T. Acton, "Spatiotemporal Gaussian feature detection in sparsely sample data with application to InSAR," *Proceedings of the SPIE Defense, Security, and Sensing,* Baltimore, Maryland, 29 Apr. – 3 May, 2013

B. S. Bruckno, A. Vaccari, E. Hoppe, W. Niemann, and E. Campbell, "Validation of Interferometric Synthetic Aperture Radar as a Tool for Identification of Geohazards and At-Risk Transportation Infrastructure," *Proceedings of the 64th Highway Geology Symposium*, North Conway, New Hampshire, Sept. 9-12, 2013

A. Vaccari, and S. T. Acton, "Spatiotemporal Gaussian feature detection in sparsely sample data with application to InSAR," *Proceedings of the SPIE Defense, Security, and Sensing,* Baltimore, Maryland, 29 Apr. – 3 May, 2013

M. Stuecheli, A. Vaccari, and S. T. Acton, "Graph cut segmentation of sparsely sampled images with application to InSAR-measured changes in elevation," *Image Analysis and Interpretation (SSIAI), 2012 IEEE Southwest Symposium on*, pp.149-152, 22-24 April 2012

Workshops

A. Vaccari, and Q. Sang, "Automated Analysis of Interferometric Synthetic Aperture Radar Images for Monitoring the Transportation Infrastructure," *1st Symposium on Cyber-Physical Systems at WVU Tech*, Montgomery, WV, May 2, 2013

S. T. Acton, M. Stuecheli, A. Vaccari, E. Hoppe, and B. Bruckno, "Model for Sinkhole detection by InSAR," *TRB Sensing Technologies*, Washington, DC, January 13, 2013

S.T. Acton, E. Hoppe, B. Bruckno, A. Bohane, and G. Falorni, "Investigating Interferometric Synthetic Aperture Radar for Transportation Infrastructure Monitoring," *TRB Sensing Technologies*, Washington, DC, January 22, 2012

Media Coverage

During the project period, the media reported on the development of our research. In particular:

- IEEE article in the *Institute*, September 9, 2013 (link)
- IEEE TV News Story (link)
- UVA Today, July 11, 2012 (link)
- ECE News, Spring 2012 (link)

Outreach

Oral presentation of our research results and software were made by Dr. Edward Hoppe of VDOT (VCITR) and Dr. Brian Bruckno of VDOT.

During the project period, reports were made to the following agencies:

- New Hampshire Department of Transportation
- New York State Department of Transportation
- Vermont Agency of Transportation
- California Department of Transportation

- Virginia Department of Transportation
- Wyoming Department of Transportation
- Colorado Department of Transportation
- Maine Department of Transportation
- Idaho Department of Transportation
- Kansas Department of Transportation
- Tennessee Department of Transportation

Future developments

In future work, the project wishes to take the research to application at the network level. Such development would provide consistent and reliable information about road subsidence, bridge monitoring, slope stability, sinkhole development and pavement condition to state departments of transportation (DOTs) in the form of geographic information systems (GIS) layer that can be seamlessly integrated within existing decision support systems with the goal of optimizing resource allocation for maintenance and inspection of the transportation infrastructure at the network level. The research team seeks to develop proactive tools providing consistent reliable information at state or county level to approach the issue of mitigation and response to early warning indicators.

Building on the success of the project reported here, brought forth by the University of Virginia team (with collaborators TRE and Virginia Center for Transportation Innovation and Research), the future study will push the use of novel space-based radar technology to detect ground deformation from the validation stage to the network implementation stage focusing on two high metropolitan areas in Virginia with the aim of providing consistent and temporally significant information on hundreds of bridge overpasses, all interstate and primary road sections, hundreds of known rock and rip-rap slopes and all karst areas close to transportation corridors with sinkhole risk. The information will be distributed to network planners as multiple layers (data, analysis, risk and reliability assessment and evaluation, risk and status indicators) within an online GIS framework. A model cost benefit analysis, adaptable to other state DOTs, will be integral part of the project deliverables as well as an information/outreach package.

References

[1] E. Bingham, *Publication 105: Physiographic Diagram of Virginia, Map, scale 1:750,000,* 1991.

[2] M. J. Bartholomew, Geology of the Greenfield and Sherando quadrangles, Virginia, Richmond, VA: Commonwealth of Virginia, Dept. of Conservation and Economic Development, Division of Mineral Resources, 1977.

[3] E. K. Rader and G. P. Wilkesm, *Publication 163: Geologic Map of the Virginia Portion of the Staunton 30x60-minute Quadrangle, Map, scale 1:100,000,* 2001.

[4] A. Ferretti, C. Prati and F. Rocca, "Permanent scatterers in SAR interferometry," *IEEE Trans. on Geoscience and Remote Sensing,* vol. 39, no. 1, pp. 8-20, Jan. 2001.

[5] A. Ferretti, A. Fumagalli, F. Novali, C. Prati, F. Rocca and A. Rucci, "A New Algorithm for Processing Interferometric Data-Stacks: SqueeSAR," *IEEE Trans. on Geoscience and Remote Sensing,* vol. 49, no. 9, pp. 3460-3470, Sep. 2011.

[6] M. Stuecheli, A. Vaccari and S. T. Acton, "Graph cut segmentation of sparsely sampled images with application to InSAR-measured changes in elevation," in *2012 IEEE Southwest Symposium on Image Analysis and Interpretation (SSIAI)*, Santa Fe, New Mexico, U.S.A., 2012.

[7] A. Vaccari, M. Stuecheli, B. Bruckno, E. Hoppe and S. T. Acton, "Detection of geophysical features in InSAR point cloud data set using spatiotemporal models," *International Journal of Remote Sensing (Accepted for publication),* vol. TBD, no. TBD, p. TBD, TBD 2013.

[8] J. Shi and J. Malik, "Normalized cuts and image segmentation," in *Computer Vision and Pattern Recognition, 1997. Proceedings., 1997 IEEE Computer Society Conference on*, 1997.

[9] X. Lin, B. Cowan and A. Young, "Model-based Graph Cut Method for Segmentation of the Left Ventricle," in *Engineering in Medicine and Biology Society, 2005. IEEE-EMBS 2005. 27th Annual International Conference of the*, 2005.

[10] B. N. Delaunay, "Sur la sphère vide," *Bulletin of Academy of Sciences of the USSR,* vol. 7, no. 6, pp. 793-800, 1934.

[11] K. A. Johnson, "Development of the Wink Sink in west Texas, U.S.A., due to salt dissolution and collapse," *Environmental Geology and Water Sciences,* vol. 14, no. 2, pp. 81-92, Sep. 1989.

[12] G. L. Turin, "An introduction to matched filters," *IRE Trans. on Information Theory,* vol. 6, no. 3, pp. 311-329, Jun. 1960.

[13] D. Ballard, "Generalizing the Hough transform to detect arbitrary shapes," *Pattern*

Recognition, vol. 13, no. 2, pp. 111-122, 1981.

[14] Sirovision, *User Guide,* 2012.

[15] W. L. Niemann, *Use of Digital Photogrammetry to Monitor Change at Selected Rock Slopes,* 2013.